

TiN Inclusion Formation during the Solidification of Stainless Steel

by

Tomomitsu Inada

S.B., University of Tokyo, Japan (1990)

Submitted to the Department of Materials Science and Engineering
in partial fulfillment of the requirements for the degree of

MASTER OF SCIENCE
in Materials Science and Engineering

at the

MASSACHUSETTS INSTITUTE OF TECHNOLOGY
June 1999

© 1999 Massachusetts Institute of Technology. All rights reserved.

Signature of Author: _____
Department of Materials Science and Engineering
May 7, 1999

Certified by: _____
Merton C. Flemings
Toyota Professor of Materials Processing
Thesis Supervisor

Accepted by: _____
Linn W. Hobbs
John F. Elliott Professor of Materials
Chairman, Department Committee on Graduate Students

TiN Inclusion Formation during the Solidification of Stainless Steel

by

Tomomitsu Inada

Submitted to the Department of Materials Science and Engineering on May 7, 1999 in partial fulfillment of the requirements for the degree of Master of Science in Materials Science and Engineering

Abstract

The formation of titanium nitride (TiN) nonmetallic inclusions during the solidification of stainless steel 409 was investigated for different concentrations of titanium and nitrogen at different cooling rates. Specimens were melted using an electromagnetic levitation facility. Rapid solidification was subsequently obtained in an increased gas flow (gas-cooling: 40 Ks^{-1}) or by casting into a liquid metal bath (quenching: 5×10^3 to $1 \times 10^6 \text{ Ks}^{-1}$).

In gas-cooled specimens containing primary TiN inclusions, the formation of equiaxed dendrite grains and early coverage of the whole surface by columnar dendrite grains were observed during solidification. Grain boundary pinning by the fine inclusions was also observed. In contrast, no effect on the microstructure was observed in the quenched specimens.

Most TiN inclusions were located along the interdendritic or intercellular spaces and had a typical cuboidal shape, although irregularly shaped particles were also observed. The average inclusion size was predominantly controlled by the secondary inclusions and showed a power law dependence on the cooling rate with an exponent of -0.190. Inclusions larger than $1 \mu\text{m}$, observed in the quenched core of the gas-cooled/quenched specimens, were primary. These inclusions grew both in size and number density with increasing holding times at the solidification plateau prior to quenching.

The kinetics of inclusion formation consisting of nucleation, growth and coarsening was evaluated from the experimental results. Primary inclusions presumably nucleate heterogeneously and their growth is presumably controlled by diffusion. Nucleation of secondary inclusions is also mostly heterogeneous. The decrease of their size with increasing cooling rate may be explained by coarsening.

Thesis Supervisor: Merton C. Flemings

Title: Toyota Professor of Materials Processing

Table of Contents

Title Page	1
Abstract	2
Table of Contents	3
List of Figures	5
List of Tables	8
Acknowledgments	9
I. Introduction	10
II. Literature Survey	12
1. Inclusion Formation	12
a) Primary Inclusions	12
b) Secondary inclusions	13
2. Microstructure Control by Inclusions	14
a) Mechanism	14
b) Grain Refining in $\gamma \rightarrow \alpha$ Transformation	15
c) Equiaxed Grain Formation in Ferritic Solidification	15
III. Experimental Procedure	19
1. Levitation Experiments	19
2. Specimen Examination	21
a) Alloy composition	21
b) Microstructure and Microsegregation	21
c) Nonmetallic Inclusions	22
IV. Calculation	28
1. Thermal Diffusion	28
2. Microsegregation	28

V. Results	33
1. Alloy Composition	33
2. Thermal History	34
3. Microstructure and Microsegregation	35
a) Microstructure	35
b) Microsegregation	38
c) Summary	39
4. Nonmetallic Inclusions	39
a) Morphology and Location	39
b) Composition	41
c) Size and Amount	42
d) Summary	45
VI. Discussion	73
1. Nucleation of Inclusions	73
2. Diffusion-Controlled Growth of Inclusions	75
a) Calculation	75
b) Growth of Primary Inclusions	76
c) Growth of Secondary Inclusions	77
3. Coarsening of Inclusions	78
a) Coarsening of Primary Inclusions	78
b) Ostwald Ripening of Secondary Inclusions	79
4. Summary	80
VII. Conclusions	89
Appendices	90
Bibliography	95
Biographical Note	97

List of Figures

Figure 1 – Equiaxed grain formation on TiN during ferritic solidification of stainless steel (Koseki, et al. [19]) -----	18
Figure 2 – Schematic diagram of the apparatus for levitation melting experiments---	26
Figure 3 – Typical Thermal history observed during gas-cooling -----	27
Figure 4 – Measured [Ti] and [N] in gas-cooled specimens and theoretical TiN solubility -----	46
Figure 5 – Numerically calculated thermal history for a gas-cooled specimen -----	48
Figure 6 –Shell thickness and fraction solid as a function of time at solidification plateau for gas-cooling-and-freezing experiments and calculation -----	49
Figure 7 – Numerically calculated thermal history for a quenched specimen: in the bulk specimen as a function of radial distance from the surface (top), near the bottom of the specimen as a function of distance from the surface (bottom) -----	50
Figure 8 – Calculated cooling rate between 1863K and 1813K in a gas-cooled specimen and a quenched specimen -----	51
Figure 9 – Microstructure of a high-Ti-alloy specimen melted and gas-cooled in 4%N ₂ -gas: the entire specimen (top) and the last portion to solidify (bottom) -----	52
Figure 10 – Microstructure of a low-Ti-alloy specimen melted and gas-cooled in 4%N ₂ -gas: the entire specimen (top) and the last portion to solidify (bottom) -----	53
Figure 11 – Microstructure of a low-Ti-alloy specimen melted and gas-cooled in no-N ₂ -gas: the entire specimen (top) and the last portion to solidify (bottom) -----	54
Figure 12 – Microstructure of a high-Ti-alloy specimen melted and gas-cooled in 4%N ₂ -gas and then quenched in In-Ga bath after holding at the solidification plateau for 3.5 s: the entire specimen (top) and equiaxed dendrite grains in the frozen core (bottom) -----	55
Figure 13 – Microstructure of a high-Ti-alloy specimen melted and gas-cooled in 4%N ₂ -gas and then quenched in In-Ga bath after holding at the solidification plateau for 6.1 s: the entire specimen (top) and an equiaxed dendrite grain in the frozen core (bottom) -----	56
Figure 14 – Microstructure of a low-Ti-alloy specimen melted and gas-cooled in 4%N ₂ -gas and then quenched in In-Ga bath after holding at the solidification plateau for 3.7 s -----	57
Figure 15 – Microstructure of a high-Ti-alloy specimen melted in 4%N ₂ -gas and quenched in In-Ga bath: the entire specimen (top) and a portion near flow lines (bottom) -----	58

Figure 16 – Microstructure of a low-Ti-alloy specimen melted in no-N ₂ -gas and quenched in In-Ga bath: the entire specimen (top) and a portion near the bottom surface (bottom) -----	59
Figure 17 – Variation of secondary dendrite arm spacing and cell spacing with cooling rate -----	60
Figure 18 – Chromium and titanium microsegregation in high-Ti-alloy specimens melted in 4%N ₂ -gas: a gas-cooled specimen (left) and a quenched specimen (right) -----	61
Figure 19 – SEM secondary electron images of inclusions in a high-Ti-alloy specimen melted and gas-cooled in 4%N ₂ -gas: [A]: a typical cuboidal particle (top) and a “dog-bone-like” particle (bottom) [B]: typical cuboidal particles and a coalescent particle (middle) [C]: a cuboidal particle with a rod at its corner [D]: agglomerated cuboidal particles [E]: a cuboidal particle showing terraces on its face [F]: strings of irregular “worm-like” particles along grain boundaries -----	62
Figure 20 – SEM secondary electron images of inclusions in a high-Ti-alloy specimen melted in 4%N ₂ -gas and quenched in In-Ga bath: [A][B]: typical cuboidal particles [C]: a string of irregular particles along an intercellular space [D]: fine irregular particles along a grain boundary -----	63
Figure 21 – Spectrum in energy dispersive X-ray spectroscopy from a cuboidal particle (edge length of 2 μm) in a high-Ti-alloy specimen melted and gas-cooled in 4%N ₂ -gas -----	64
Figure 22 – EPMA images of a large inclusion in a high-Ti-alloy specimen melted and gas-cooled in 4%N ₂ -gas: backscattered electron image (top-left) and element mapping images of iron, titanium and nitrogen -----	65
Figure 23 – Inclusion size distribution in a high-Ti-alloy specimen melted and gas-cooled in 4%N ₂ -gas: small inclusions (< 1 μm) observed by SEM (top) and large inclusions (≥ 1μm) observed by optical microscopy (bottom) -----	66
Figure 24 – Inclusion size distribution in a low-Ti-alloy specimen melted and gas-cooled in 4%N ₂ -gas: small inclusions (< 1 μm) observed by SEM (top) and large inclusions (≥ 1μm) observed by optical microscopy (bottom) -----	67
Figure 25 – Inclusion size distribution in a high-Ti-alloy specimen melted and in 4%N ₂ -gas and quenched in In-Ga bath: in the bulk of specimen 1 to 2 mm from the bottom surface (top), and in a subsurface region 200μm from the bottom surface (bottom) -----	68

Figure 26 – Comparison of [N] contained in TiN in specimens melted in 4%N ₂ -gas measured by microscopy and that measured by wet chemical analyses, assuming that all titanium insoluble to sulfuric acid was TiN -----	69
Figure 27 – Variation of average TiN inclusion size with cooling rate in high-Ti-alloy specimens melted in 4%N ₂ -gas -----	70
Figure 28 – Variation of inclusion size distribution ($\geq 1 \mu\text{m}$) with holding time at solidifying plateau in the frozen core of high-Ti-alloy specimens melted and gas-cooled in 4%N ₂ -gas and then quenched in In-Ga bath -----	71
Figure 29 – Increase of primary TiN inclusions ($\geq 1 \mu\text{m}$) as a function of holding time at the solidifying plateau in the frozen core of high-Ti-alloy specimens melted and gas-cooled in 4%N ₂ -gas and then quenched in In-Ga bath: the amount of TiN inclusions expressed by contained [N] (top), and the largest particle size (bottom) -----	72
Figure 30 – Increase of the supersaturation factor η due to the microsegregation along with the critical supersaturation needed for homogeneous nucleation of TiN particles in the melt -----	82
Figure 31 – Concentration profile near a growing particle -----	83
Figure 32- Calculated particle diameter during diffusion-controlled growth of primary TiN inclusions in the melt for high-Ti-alloy: without solute depletion by the TiN formation [line (1)], assuming constant number density of particles of $1.14 \times 10^4 \text{ mm}^{-3}$ [line (2)], and measured largest inclusion size in gas-cooled-and-quenched specimens vs. holding time at the solidification plateau [line (3)]	84
Figure 33- Calculation results of growth related parameters of secondary TiN inclusions in gas-cooled specimens: variation of [Ti] (a) and [N] (b), as a function of fraction solid, and increase of particle size with time (c) -----	85
Figure 34- Calculation results of growth related parameters of secondary TiN inclusions in the quenched specimen of high-Ti-alloy: variation of [Ti] (a) and [N] (b) as a function of fraction solid, and increase of particle size with time (c)--	86
Figure 35- Variation of solubility of spherical TiN particles vs. diameter, expressed by the ratio of the concentration product for particle divided by that corresponding to planar TiN, assuming interfacial tension of 0.8 Nm^{-1} -----	87
Figure 36- Ostwald ripening of secondary TiN inclusions: calculated curve of average particle diameter vs. time, assuming the initial average diameter of $0.01 \mu\text{m}$ and the interfacial tension of 0.8 Nm^{-1} , and experimental points representing average inclusion size observed in gas-cooled and quenched specimen reported vs. local solidification time t_f -----	88

List of Tables

Table 1 – Crystallographic misfit of principal inclusions relative to iron [11] -----	17
Table 2 – Composition of base materials (wt%) -----	25
Table 3 – Values of the parameters used in the calculation of thermal histories -----	31
Table 4 – Values of the parameters used in the calculation of microsegregation -----	32
Table 5 – Interaction coefficients used in the calculation of TiN solubility [31] -----	47
Table 6 – Values of the parameters used in the calculation of inclusion formation --	81

Acknowledgements

I would like to express my deepest gratitude to Professor Merton C. Flemings, for the opportunity to join his group and for his guidance throughout my study. I sincerely appreciate him for granting me a great deal of autonomy in both choosing and carrying out this work. I have always felt very trusted under his supervision.

I owe a great deal to the Solidification Group, whose members have been a constant source of support during my stay at MIT. In particular, I would like to thank Professor Theo Kattamis for the many hours spent to support me. He was a great help in examining microstructure and he also proofread the drafts of this thesis and gave me various suggestions. My deep gratitude also goes to Dr. Anacleto de Figueredo, who patiently checked and corrected my English writing. He has been a really good English teacher. I would also like to thank Dr. Douglas M. Matson and Mr. Quoc C. Bui, who built up the levitation facility and allowed me use that in this work. I would also thanks to Mr. Jim Yurko. Dr. Akira Kato, Mr. Xiyu Zhao, Mr. Shou-Yi Chang, Ms. Stacey Rochford and all other past or present members for their help and friendship. I really enjoyed working with them.

I am also grateful to Nippon Steel Corporation for giving me the opportunity and financial support to study abroad for two years. Special gratitude should be expressed to Professor Tasuku Fuwa for his support during my stay at MIT, Dr. Toshihiko Koseki and Mr. Ryusuke Miura for providing materials and for chemical analyses in the experiments.

Finally, I dedicate this work to my wife Yoshiko, who have constantly supported me for eleven years, and to my lively son Mizuki.

I. Introduction

As the demand for steel with better quality and mechanical properties continues to grow, significant research efforts on nonmetallic inclusions have been undertaken. In general, inclusions are undesirable because they lead to defects in products, and great efforts have been made to efficiently remove them. However, some inclusions are useful, since they act as grain refiners by promoting the nucleation of ferrite during solidification and the transformation of austenite to ferrite. Fine particles also improve mechanical strength by preventing grain growth during hot rolling and by precipitation hardening. The use of inclusions to control macrostructure is more important in strip casting, a process that is replacing conventional continuous casting and hot rolling processes that had an essential role in microstructural control of sheet steel products. It is, therefore, important to obtain desirable inclusions with proper composition and size and to understand the mechanism of their formation.

The formation of inclusions during solidification has been studied by many researchers with special emphases placed on continuous casting and welding process; however, the precise mechanism is far from being understood, since it is affected by many process parameters. Furthermore, primary inclusions that existed before solidification are generally difficult to distinguish from secondary inclusions that formed during solidification. The size of secondary inclusions is reported to decrease with increasing cooling rate. However, only few studies have been carried out at cooling rates higher than $1,000 \text{ Ks}^{-1}$, which are typical of strip casting.

The purpose of the present work was to investigate the mechanism of inclusion formation under relatively simple conditions, by mean of levitation melting. A wide range of cooling rates was achieved by gas cooling and quenching. Titanium nitride (TiN) was selected because its solubility varies widely with temperature and the nitrogen concentration in the matrix is relatively easy to control compared to that of oxygen. The kinetics of inclusion formation, which consists of nucleation, growth and coarsening, was investigated by observing inclusions contained in specimens

processed under various experimental conditions. The effect of TiN inclusions on the microstructure was also investigated, since it is known to promote ferrite formation and primary TiN inclusions may act as nucleants during solidification, leading to a fine equiaxed structure, which is usually highly desirable.

II. Literature Survey

During cooling of a metallic melt containing nonmetallic element impurities, particulate nonmetallic inclusions may nucleate and grow [1]. Primary inclusions are defined as those which form within the melt prior to nucleation of the dendritic or cellular metallic alloy phase. Secondary inclusions are those which nucleate and grow within the interdendritic or intercellular spaces, due to a solute rejection and gradual enrichment of constituent elements therein. A third type of inclusions may also form in some cases by solid state precipitation within the metallic alloy phase.

1. Inclusion Formation

The kinetics of inclusion formation consists of three steps: nucleation, growth and coarsening. When solute supersaturation becomes sufficient to overcome the nucleation barrier, nucleation and subsequent growth of inclusions occur. Coarsening may take place simultaneously or after equilibrium is reached. It is important to find which is the slowest kinetic process that controls the inclusion size and number density. A number of studies were carried out on this subject and various mechanisms have been proposed to explain their results.

a) Primary Inclusions

Kluken and Grong [2], investigated oxide inclusion coarsening in low alloy steel arc weld spots. The authors concluded that the average inclusion diameter increased proportionally to the cubic root of retention time in the cold zone of the weld pool, where steel was cooled but still in the liquid state. It was established that Ostwald ripening (diffusional coarsening) was the inclusion coarsening mechanism. Babu, et al. [3], examined oxide inclusions in low alloy steel by holding samples in the molten state in a Gleeble thermomechanical simulator for different lengths of time. The coarsening rate was very high and inclusions as large as 100 μm in diameter were detected after an isothermal hold of 60 s. Since the oxygen concentration, $[\text{O}]$, in

equilibrium with the oxide inclusions was low (1×10^{-3} wt%), Ostwald ripening would have been too slow to explain their results. They concluded that collisional coalescence, enhanced by fluid flow in the pool was responsible for the observed sizes.

In the above studies, it was assumed that equilibrium between oxide inclusions and matrix prevailed before initiation of coarsening. Formation of secondary inclusions during solidification was not taken into account, because it was difficult to distinguish them from the primary inclusions.

b) Secondary Inclusions

The cooling rate dependence of inclusion size during solidification was investigated by Brower [4]. Levitation-melted Fe-0.05wt%Si specimens were oil-quenched or chill-cast in order to obtain large cooling rates (10^2 to 10^3 Ks⁻¹). Inclusions were very fine and their size distribution and number per unit area (inclusion number density) were then studied by scanning electron microscopy. The average inclusion diameter was reported to be 0.530 μm in oil-quenched specimens and 0.099 μm in chill-cast specimens, which was very small compared to the size of inclusions in the master alloy (2.8 μm).

Oxide inclusion formation during solidification of titanium deoxidized low alloy steel was studied by Goto, et al [5,6]. The authors examined inclusions consisting mainly of Ti_2O_3 , which formed during solidification at a cooling rate of 0.1 to 100 Ks⁻¹, obtained in continuous casting and rapid solidification processing, respectively. In the rapidly cooled sample (100 Ks⁻¹), the authors found a large number of inclusions smaller than 1 μm . In contrast, inclusions as large as 10 μm were observed in the center of a cast slab (0.1 Ks⁻¹). They proposed a diffusion-controlled growth model in which the number of inclusions was assumed constant (no new nucleation or coarsening). In their model, inclusion growth was promoted by supersaturation of the product $[\text{Ti}]^2[\text{O}]^3$ due to microsegregation and ceased when the

supersaturation was relieved by the inclusion formation. The supersaturation is, in this case, expressed by

$$\eta = \frac{[\text{Ti}]^2 [\text{O}]^3}{L_{\text{Ti}_2\text{O}_3}} \quad (1)$$

where $L_{\text{Ti}_2\text{O}_3}$ is the solubility product.

The formation of TiN inclusions during solidification of a low alloy steel was investigated by Kunze, et al. [7]. Small specimens (0.5 g) of ferritic low alloy steel ([Ti]:0.051 wt%, [N]:0.008 to 0.016 wt%) were melted by induction and examined after being solidified by gas-cooling at a cooling rate of 25 Ks⁻¹. Primary inclusions could not form because the concentration product [Ti][N] was smaller than the solubility product. In the case of high [N] (0.016 wt%), inclusions as large as 0.5 to 1.0 μm were found in interdendritic spaces, where titanium segregation had occurred. In contrast, few inclusions could be found in the case of low [N] (0.008 wt%), even though the product [Ti][N] led to interdendritic supersaturation. This difference was explained by a nucleation theory, which predicted the need of a high degree of supersaturation for homogenous nucleation of inclusions in the melt. The required supersaturation:

$$\eta = \frac{[\text{Ti}] [\text{N}]}{L_{\text{TiN}}} \quad (2)$$

was estimated to be 20 to 30.

2. Microstructure Control by Inclusions

a) Mechanism

It is widely known that some inclusions serve as effective nucleation sites in matrix phase transformations. Various theories were proposed to explain why certain inclusions promote nucleation. The most widely accepted mechanism is that proposed by Turnbull and Vonnegut [8], in which a smaller crystallographic misfit between inclusions and nucleating new matrix phase is preferred because the energy barrier for

nucleation of inclusions is usually smaller in such cases. Bramfitt [9] and Ohashi, et al. [10], confirmed Turnbull's theory by measuring the possible undercooling during solidification of steels containing various inclusions. A smaller undercooling was measured for inclusions of smaller misfit relative to ferrite, such as titanium nitride (TiN). Crystallographic misfit of common inclusions relative to ferrite and austenite are listed in Table 1 [11]. TiN is one of the effective nucleants of ferrite because it has a cubic NaCl structure with a lattice parameter of 4.24173\AA , which is close to a diagonal length of a ferrite lattice ($2.8664\text{\AA} \times 2^{1/2} = 4.0537\text{\AA}$).

b) Grain Refining in $\gamma \rightarrow \alpha$ Transformation

One of the typical applications of inclusions for microstructure control can be found in the welding process. It is widely known that the toughness of heat affected zones in steel welds can be improved by the presence of acicular ferrite, a fine acicular structure that grows randomly along different directions. Various inclusions, including TiN, have been reported to be effective for nucleation of acicular ferrite from austenite [12, 13].

High strength low alloy (HSLA) steel is another example of the use of inclusions for microstructure control. In this case, titanium, vanadium and niobium are intentionally added, and fine carbonitrides are precipitated by heat treatment [14, 15, 16]. The large precipitates promote the ferrite formation while the fine precipitates depress the austenite grain coarsening during hot rolling of HSLA steel, yielding finely-grained products with high strength.

c) Equiaxed Grain Formation in Ferritic Solidification

The effectiveness of TiN to promote ferrite nucleation has also been reported during solidification. Villafuerte, et al. [17], reported that equiaxed grains nucleated preferentially on TiN inclusions in arc weld pools of ferritic stainless steel ([Ti]:0.30 to 0.42 wt%, [N]:0.0072 to 0.0171 wt%). They also provided a more direct confirmation

of the role of TiN in another experiment, where the equiaxed grain structure was observed in stationary arc welds with TiN particles seeded into the weld pool, while the entire structure was columnar without TiN particles.

Koseki, et al. [18, 19], also studied the formation of equiaxed grains in the ferritic stainless steel welds, concluding that the equiaxed grains formed only when the concentration product $[Ti][N]$ led to supersaturation at or above the liquidus temperature. In this condition, primary inclusions could form and act as nucleation sites for ferritic solidification. The concept of equiaxed grain formation on TiN during ferritic solidification is illustrated in Figure 1.

Table 1 – Crystallographic misfit of principal inclusions relative to iron [11]

Inclusion	Crystal type	Lattice parameter c (Å)	Lattice parameter a (Å)	Misfit with ferrite * (%)	Misfit with austenite * (%)
MnS	Cubic	5.224		28.9	1.3
AlN	Hexagonal	3.1114	4.9792	8.5	3.5
TiN	Cubic	4.24173		4.6	16.3
Al ₂ O ₃	Hexagonal	4.758	1.2991	17.4	7.7
SiO ₂	Tetragonal	4.9732	0.69236	22.7	3.6
TiC	Cubic	4.3274		6.8	16.1
VN	Cubic	4.13916		2.1	13.5
BN	Hexagonal	2.50441	0.66562	12.6	31.3
Ti ₂ O ₃	Hexagonal	5.139	1.3659	26.8	0.4
NbC	Cubic	4.4698		10.3	13.3
NbN	Hexagonal	2.96	1.127	3.3	18.8
Ferrite	Bcc	2.8664			
Austenite	Fcc	3.6468			

* Misfit is the smallest value of the following;

$$\frac{|a_{inc.} - a_{Fe}|}{a_{Fe}}, \frac{|a_{inc.} - \sqrt{2} \cdot a_{Fe}|}{\sqrt{2} \cdot a_{Fe}}, \frac{|c_{inc.} - a_{Fe}|}{a_{Fe}} \text{ OR } \frac{|c_{inc.} - \sqrt{2} \cdot a_{Fe}|}{\sqrt{2} \cdot a_{Fe}}$$

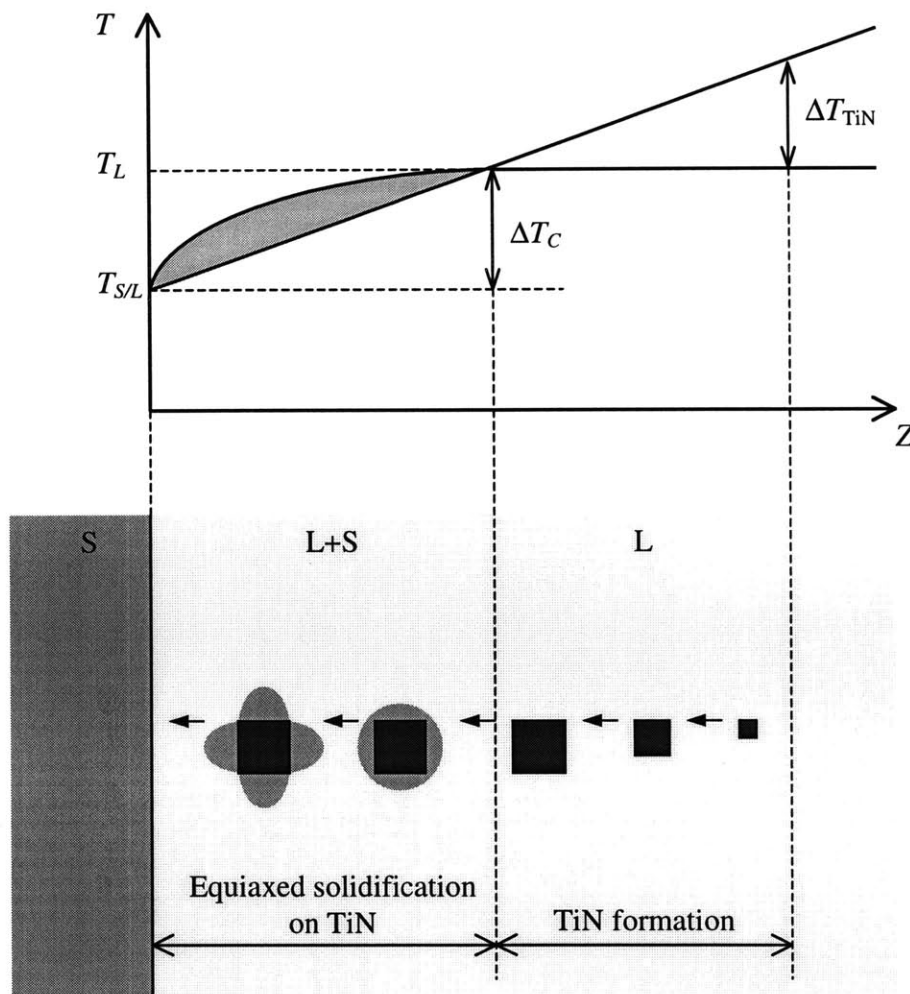


Figure 1 – Equiaxed grain formation on TiN during ferritic solidification of stainless steel (Koseki, et al. [19])

III. Experimental Procedure

1. Levitation Experiments

Commercial 409 ferritic stainless steel with two different titanium contents was used in the experiments. Base alloys were prepared at Nippon Steel Corporation, Japan, and cut from thick hot rolled plates. Analyzed concentrations of alloying elements are listed in Table 2. The titanium concentration in the materials was 0.24 wt% and 0.056 wt%. Those materials are hereafter referred to as high-Ti-alloy and low-Ti-alloy, respectively. The typical mass and diameter of the experimental specimens were 1.1 ± 0.1 g and 6.7 ± 0.2 mm, respectively.

Figure 2 exhibits a schematic representation of the experimental apparatus used in the present work, which consisted of a levitation melter, a purging system, and a temperature measuring system. The power source consisted of a 10 kW radio-frequency current generator operating at a nominal frequency of 430 kHz. Energy was supplied to the specimen by a copper tubing-split induction coil in the levitation chamber. The coil had an inner diameter of 16 mm with six lower primary turns in a double loop pattern and two upper reverse-wound turns to augment stability. The chamber was connected to a vacuum pump and a gas inlet, which were used to control the atmosphere. Before levitation melting, the chamber was purged twice. A continuous gas flow was provided during melting to control the temperature and maintain a reducing atmosphere. The pressure in the chamber was maintained at 5kPa above ambient. A mixture of 4 vol% hydrogen, 4 vol% nitrogen, and helium was used in experiments with TiN formation. A mixture of 4 vol% hydrogen and helium was used in experiments without TiN formation. These mixtures of gases are referred to hereafter as “4%N₂-gas” and “no-N₂-gas”, respectively.

Temperature was measured using a silicon photodiode two-color pyrometer operating at near-infrared wavelength bands centered at 0.81 and 0.95 μm . Pyrometric data was monitored and recorded by the data acquisition software at a rate of 100 Hz. Calibration of the thermal measurements was performed a priori in the same way as

detailed in the previous work [20]. The linear signal-temperature relationship was evaluated in absence of TiN formation. When TiN formed and covered the droplet surface, a shift in emissivity was observed. Thus, the linear signal-temperature relationship was no longer valid. TiN formation on the specimen surface was easily confirmed after cooling down to the ambient temperature because the surface was uniquely colored yellow by a particulate TiN surface layer. In the present work, gas cooling was sufficiently rapid, thus a TiN surface layer formed only after cooling down to the liquidus temperature and recalibration was not necessary.

Specimens were positioned into the chamber on individual sample holders made with boron nitride (BN). The sample holders were placed on a carousel along with a gallium-22wt%indium liquid metal bath for quenching. Typically, specimens were levitated, melted, and superheated to 100 K above the liquidus temperature.

After holding at a specified temperature (holding temperature) for about 300 s, specimens were cooled by increasing the gas flow rate while being levitated. Holding times of greater than 30 s were sufficient to obtain the equilibrium nitrogen concentration, [N] with the atmosphere as shown in Appendix A. Typical cooling rates of 40 to 50 Ks⁻¹ were observed by pyrometry. This process is hereafter referred to as “gas-cooling”. Undercoolings of 20 to 150 K and subsequent recalescence were often observed by pyrometry in experiments with low-Ti-alloy specimens. Specimens with large degree of undercoolings (> 30 K) were not examined because such large undercoolings led to different microstructures.

In order to preserve the solidifying structure at different times during gas-cooling, some specimens were gas-cooled to the liquidus temperature and held at the solidification plateau for various times prior to quenching. Quenching was accomplished by simply cutting the power supply, so that specimens fell into the liquid metal bath when the electromagnetic levitation force was no longer applied. The distance between the levitated droplet and liquid metal bath was approximately 3 cm. This process is referred to as “gas-cooling-and-freezing”. In order to achieve higher

cooling rates, other specimens were directly quenched from the higher holding temperature into the In-Ga bath. This process is referred to as “quenching”.

A typical thermal history measured by pyrometry in a gas-cooling experiment is shown in Figure 3 with arrows indicating the points from which specimens were quenched into the liquid metal bath during the quenching and gas-cooling-and-freezing experiments.

2. Specimen Examination

a) Alloy Composition

Gas-cooled and gas-cooled-and-frozen specimens had approximately spherical shapes with a small cavity at the bottom side. Quenched specimens had approximately polar cap shapes and irregular shapes at the topside. Samples were sectioned transversely into three parts. The polished sections examined were the surfaces of the plate-like middle parts, about 2mm thick. The two remaining parts were used for chemical analyses, which were carried out at Kyushu Techno Reseach, Co., Japan. Nitrogen concentration, [N], was measured by the thermal conductometric method after fusion in an argon current. Similarly, oxygen concentration, [O], was measured by the infrared absorption method after fusion in an argon current. Titanium concentration in solid solution and in its compound state (nitride, oxide, and carbide) was assessed by wet chemical analysis, in which a specimen was dissolved in an aqueous solution of sulfuric acid. Following filtration, the amount of both soluble and insoluble (in a compound state) titanium was measured by the ICP (induction-Coupled-Plasma) method. The concentration of titanium in the soluble and insoluble states is hereafter referred to as “soluble [Ti]” and “insoluble [Ti]”, respectively.

b) Microstructure and Microsegregation

The middle section of the specimen was mounted in an electrically conductive resin, mechanically polished using alumina suspensions down to 0.05 μm , and then

electrolytically etched at 6 V for 30 to 60 s in an aqueous solution of 10 vol% sulfuric acid. This etching procedure reveals both microsegregation generated during solidification and grain boundaries. The structures were examined by optical microscopy.

Chromium and titanium microsegregation in the gas-cooled and quenched structure of high-Ti-alloy was measured by electron probe microanalysis (EPMA), using JEOL JXA-733 Superprobe in the MIT Electron Microprobe facility. In the gas-cooled structure, measurements were carried out at 4 points (6 μm apart), ranging from the center out to surface of a secondary dendrite arm. In the quenched fine structure, measurements were carried out at 3 points (2 μm apart) between the cell center and surface. Operating conditions of EPMA were: acceleration voltage of 15 kV; beam current of 1 nA; spot size of 1 μm ; and counting time of 5 s for iron, 20 s for chromium, and 40 s for titanium.

c) Nonmetallic Inclusions

Inclusions were observed using scanning electron microscopy (SEM) and optical microscopy. A heavily etched sample for microstructure observation was subsequently mechanically polished again and electrolytically etched at 6 V for about 4 s in an aqueous solution of 10 vol% sulfuric acid. Slight etching made inclusions easy to be distinguished in SEM; it also revealed relative positions of inclusions within the microstructure.

SEM observation was carried out using JEOL 6320FV Field Emission Scanning Electron Microscope in the Center for Materials Science and Engineering in MIT. Operating conditions were: acceleration voltage of 15 kV; probe current of 60 pA; and working distance of 15 mm. Inclusions larger than 0.050 μm were measured while line scanning on the specimen at a magnification of 12,000 \times . The scanned area in each observation was 300 to 10,000 μm^2 depending on the existing inclusion size and number density. Total number of observed inclusions in each observation was 30 to

100 except in the quenched specimens of low-Ti-alloy, where only 5 inclusions could be found.

Inclusions larger than 1 μm were observed by optical microscopy, because they were so infrequent that they might not appear within the area scanned by SEM. More than twenty randomly chosen areas of 0.026 mm^2 were observed at a magnification of 200 \times . TiN inclusions were easily distinguishable by optical microscopy, because of their unique yellow color and angular shape. The total number of inclusions in a given measurement was in a range from 30 to 150, except in the quenched specimens, which contained only fine inclusions smaller than 0.5 μm .

The composition of the inclusions was examined by electron dispersive X-ray spectrometry (EDS). In spectra of titanium nitride particles, titanium was easily distinguishable by looking at its K_α peak at 4.508 keV. By contrast, since the K_α peak for nitrogen at 0.392 keV is indistinguishable from the L1 peak for titanium at 0.395 keV, the presence of nitrogen in the inclusions could not be detected directly from EDS. In this case, elemental X-ray images of iron, titanium and nitrogen in large inclusions were taken by EPMA. Concentration mapping was possible only for inclusions larger than 1 μm , and the smaller inclusions required point analyses. Operating EPMA parameters were: acceleration voltage of 15 kV; beam current of 10 nA; spot size of 1 μm ; number of pixels of 500 \times 500; and dwell time of 5×10^{-3} s per pixel.

To obtain the inclusion size distribution, the longest edge of the quadrangular, pentagonal or hexagonal inclusion particles was chosen as a characteristic inclusion size, because the longest edge most likely coincided with the edge of the TiN cuboidal particle in three dimensions. The particle size distribution determined on a polished surface was then converted to a volume distribution by the following equation:

$$N_{3D}(a) = \frac{N_{2D}(a)}{a} \quad (3)$$

where a is the edge length of the cuboidal inclusion particle as observed on a cross-section, $N_{3D}(a)$ and $N_{2D}(a)$ are, respectively, the numbers of particles of size a per unit volume and per unit area. The average size in three dimensions is equal to the harmonic mean of the two dimensional size, expressed by

$$\bar{a}_{3D} = \left(N / \sum \frac{1}{a} \right)_{2D} \quad (4)$$

where \bar{a}_{3D} is the three dimensional average inclusion size. Theoretically, the inclusion size distribution is independent of the sectioning plane. Distinct small inclusions may be found on the next sectioning plane, while the same large inclusion is observed on many sectioning planes. Therefore, the population density of smaller inclusions becomes relatively higher when converted to the three dimensional distribution.

The amount of inclusions was calculated from their total area fraction, which was equal to the volume fraction when the polished plane was completely flat and intersected the inclusions randomly. Inclusions with triangular shape and other irregular shapes were not included in the size distribution, but included in the total area fraction. It should be noted that a large number of inclusions had irregular “worm-like” shapes, lying along the interdendritic or intercellular spaces.

Table 2 – Composition of base materials (wt%)

	high-Ti-alloy	low-Ti-alloy
C	0.0094	0.0097
Si	0.37	0.3
Mn	0.36	0.32
P	0.018	0.016
S	0.001	0.001
Cr	10.93	11.06
Ti	0.24	0.056
Al	0.013	0.011
N	0.0135	0.015
O	0.002	0.002

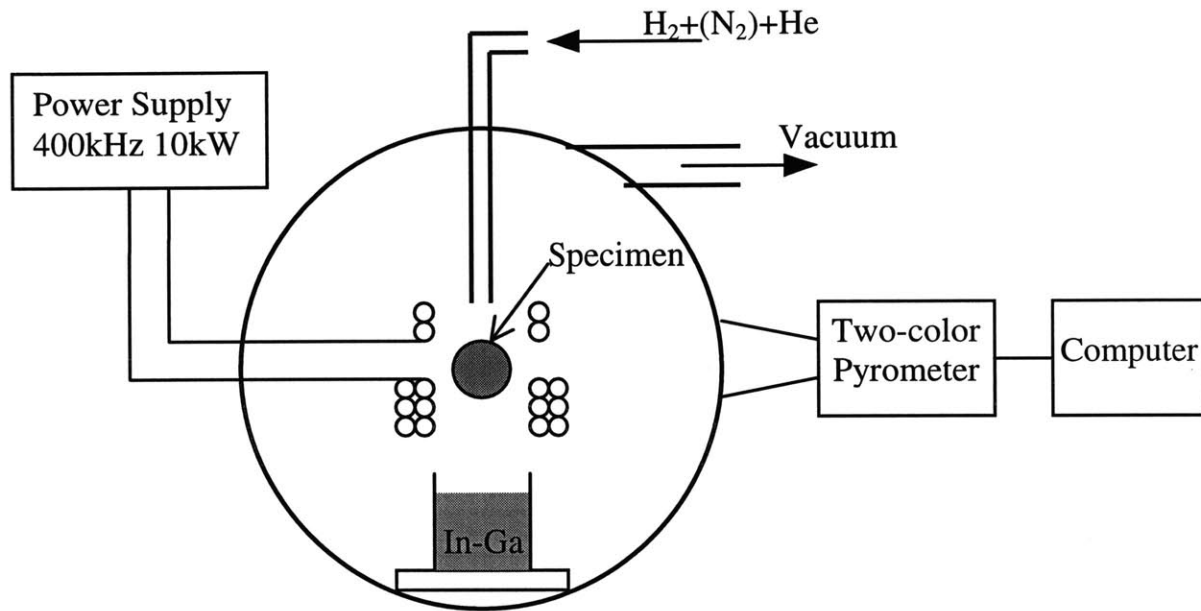


Figure 2 – Schematic diagram of the apparatus for levitation melting experiments

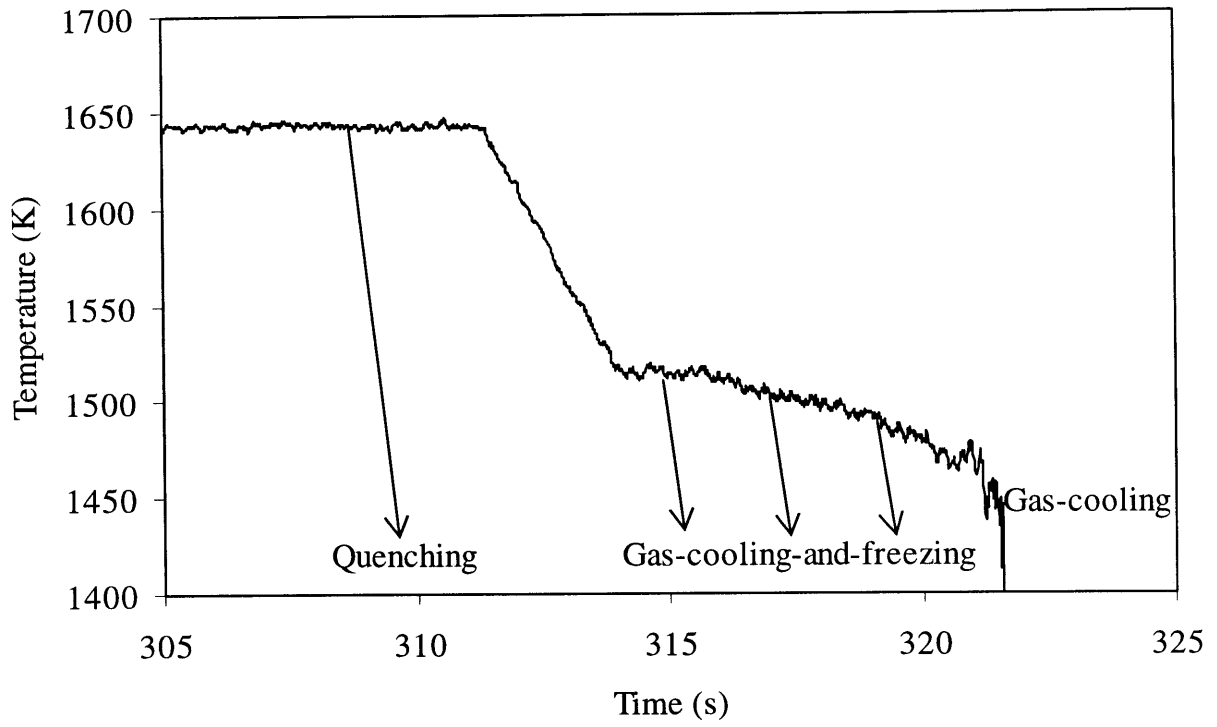


Figure 3 – Typical Thermal history observed during gas-cooling

IV. Calculation

1. Thermal diffusion

Thermal histories of the whole specimens were calculated by a finite difference method [21] for both gas-cooling and quenching experiments. Spherical symmetry was assumed to be maintained during specimen cooling. In the calculation for the gas-cooling process, the heat of fusion generated during solidification was taken into account by increasing the temperature of each segment cooled below the liquidus temperature until it solidified completely. More details are included in Appendix B.

The numerical data used are listed in Table 3. In the gas-cooling process, the heat transfer coefficient between the specimen surface and the atmosphere was chosen as $300 \text{ Wm}^{-2}\text{K}^{-1}$. This value provided the best fit to the measured cooling rate at the specimen surface. In the quenching process, the heat transfer coefficient was assumed to be $1 \times 10^6 \text{ Wm}^{-2}\text{K}^{-1}$. This value is often adopted for rapid solidification processes such as melt spinning, strip casting and splat cooling, where a good contact is achieved between the solidifying material and the substrate [22, 23, 24]. The time step Δt and the thickness of a shell segment Δr in the case of gas-cooling were $1 \times 10^{-3} \text{ s}$ and $2.5 \times 10^{-4} \text{ m}$, respectively. In the case of quenching, those values were smaller, $1 \times 10^{-4} \text{ s}$ and $5 \times 10^{-5} \text{ m}$, respectively, because of the higher cooling rate.

2. Microsegregation

Microsegregation of solute titanium and nitrogen in the interdendritic or intercellular spaces was calculated by following a model introduced by Bower, Brody and Flemings [27]. The equation of solute mass balance was expressed as

$$\underbrace{(C_L - C_S^*)}_{\text{solute rejected at interface}} \frac{dy^*}{dt} = \underbrace{(1 - y^*)}_{\text{solute increase in liquid}} \frac{dC_L}{dt} + D_S \underbrace{\left(\frac{\partial C_S^*}{\partial y} \right)}_{\text{solute back diffusing in solid}} \Big|_{y=y^*} \quad (5)$$

where C_L and C_S^* are solute concentrations in the liquid and in solid at the solid-liquid interface, respectively, D_s is diffusion coefficient in solid and y^* is the interface position within the volume element of length l ; hence, the fraction solid is y^*/l . Assuming that solute gradient at the interface is independent of diffusion in solid,

$$\left(\frac{\partial C_S^*}{\partial y} \right)_{y=y^*} = \frac{dC_S^*}{dy^*} \quad (6)$$

Also assuming that the rate of dendrite thickening is constant, then

$$\frac{dy^*}{dt} = \frac{l}{t_f} \quad (7)$$

where t_f is local solidification time. Eq. (5) can lead to a differential equation of C_L and fraction solid f_s :

$$\frac{1}{C_L} dC_L = \frac{1-k}{1+\alpha k - f_s} df_s \quad (8)$$

where α is a back diffusion parameter defined as

$$\alpha = \frac{D_s t_f}{l^2} \quad (9)$$

Eq. (8) has the well-known analytical solution:

$$C_L = C_0 \left(1 - \frac{f_s}{1+\alpha k} \right)^{k-1} \quad (10)$$

However, in the present work, Eq. (8) was numerically calculated, since solute depletion by inclusion formation was taken into account.

Parameter values used are listed in Table 4. Local solidification time was estimated by

$$t_f = \frac{\Delta H_f}{C_p \dot{T}} \quad (11)$$

where ΔH_f is enthalpy of fusion and C_p is specific heat and \dot{T} is the cooling rate without considering heat of fusion generated. Values of t_f in the gas-cooled structure and quenched structure were 6.88 s and 0.0739 s, respectively. The length of solidification path l was estimated to be one half of the characteristic length of

solidification structure, a dendrite arm spacing of 45 μm in the gas-cooled structure and a cell spacing of 6 μm in the quenched structure. Calculation step Δf_s , was chosen to be 0.01. This step was small enough to achieve a good agreement with the analytic solution of Eq. (10) in absence of inclusion formation.

Table 3 – Values of the parameters used in the calculation of thermal histories

parameter		value	ref.
H	Heat transfer coefficient in gas-cooling	$300 \text{ W m}^{-2} \text{ K}^{-1}$	
	Heat transfer coefficient in quenching	$1 \times 10^6 \text{ W m}^{-2} \text{ K}^{-1}$	[22],[23],[24]
k	Thermal conductivity	$35 \text{ W m}^{-1} \text{ K}^{-1}$	[25]
C_p	Specific heat of liquid	$5.74 \times 10^6 \text{ J m}^{-3} \text{ K}^{-1}$	[25]
ΔH_f	Enthalpy of fusion	$1.811 \times 10^9 \text{ J m}^{-3}$	[25]
T_L	Liquidus temperature	1788 K	[26]
T_S	Solidus temperature	1767 K	[26]
T_∞	Ambient temperature	293 K	

Table 4 – Values of the parameters used in the calculation of microsegregation

parameter		value	ref.
$\rho(\text{Ti})$	Density of TiN	5240 kg m ⁻³	
$\rho(\text{Fe})$	Density of liquid iron	7000 kg m ⁻³	
$M(\text{Ti})$	Mass number of Ti	47.9	
$M(\text{N})$	Mass number of N	14	
$C_{inc}(\text{Ti})$	Concentration of Ti in TiN	4055 kg m ⁻³	
$C_{inc}(\text{N})$	Concentration of N in TiN	1185 kg m ⁻³	
$k(\text{Ti})$	Equilibrium partition ratio of Ti	0.14	[28]
$k(\text{N})$	Equilibrium partition ratio of N	0.28	[28]
$D_S(\text{Ti})$	Diffusion coefficient of Ti in solid iron (at 1788 K)	$6.8 \times 10^{-3} \times e^{-261000/RT}$ m ² s ⁻¹ (1.59×10^{-10} m ² s ⁻¹)	[29]
$D_S(\text{N})$	Diffusion coefficient of N in solid iron (at 1788 K)	$4.8 \times 10^{-5} \times e^{-159000/RT}$ m ² s ⁻¹ (1.08×10^{-9})	[30]
T	Temperature	1788 K	
C_p	Specific heat of liquid	5.74×10^6 J m ⁻³ K ⁻¹	[25]
ΔH_f	Enthalpy of fusion	1.811×10^9 J m ⁻³	[25]
\dot{T}	Cooling rate in gas-cooling	45.85 K s ⁻¹	
	Cooling rate in quenching	4272 K s ⁻¹	
t_f	Local solidification time in gas-cooling	6.88 s	
	Local solidification time in quenching	0.0739 s	
L	Dendrite arm spacing in gas-cooled structure	22.5 μm	
	Cell spacing in quenched structure	3.0 μm	

V. Results

1. Alloy Composition

The nitrogen and titanium concentrations in the specimens are plotted in Figure 4 along with the solubility curve of TiN calculated by the following equation [31]:

$$\log(a_{Ti} \cdot a_N) = -\frac{19800}{T} + 7.78 \quad (12)$$

where a_i is Henrian activity of solute i with respect to a hypothetical 1 wt% solution. [O] was assumed to be 0.0020 wt% at any temperature. Interaction coefficients used in the activity calculation are listed in Table 5.

In the experiments with 4%N₂-gas, nitrogen content was higher than 0.015 wt%. In the high-Ti-alloy melted in 4%N₂-gas below 1838 K (50 K above the liquidus temperature), the concentration product [Ti][N] exceeded the saturation limit, hence TiN would form in equilibrium. In the low-Ti-alloy, supersaturation occurred only when the specimen was undercooled to below 1738 K (undercooling of 50 K). The validity of assuming the theoretical solubility was approximately demonstrated by the following observations:

- 1) When high-Ti-alloy specimens melted in 4%N₂-gas were very slowly gas-cooled (5 Ks⁻¹) to about 1833 K, the ratio of two colors in the pyrometry changed due to the formation of a TiN surface layer.
- 2) Low-Ti-alloy specimens melted in 4%N₂-gas could not be undercooled below 1738 K (undercooling of 50 K), while high-Ti-alloy specimens melted in 4%N₂-gas could not be undercooled at all. Both alloys could be easily undercooled to below 1688 K (undercooling of 100 K) when melted in no-N₂-gas. Since such a large undercooling could be achieved only in absence of heterogeneous nucleation sites and TiN is theoretically the first compound phase to precipitate for these alloy compositions, it is reasonable to assume that TiN formed near 1738 K in low-Ti-alloy specimens melted in 4%N₂-gas and acted as a nucleation site during solidification.

2. Thermal History

Calculated cooling curves in a gas-cooled specimen are shown in Figure 5. Solidification began after about 2 s of gas-cooling. The cooling rate was nearly uniform throughout the specimen before the beginning of solidification, which meant that the thermal diffusion process approached steady state. It took about 8 s for the center of the specimen to solidify.

To verify the calculation, the solid shell advancing from the surface to the center of the specimen was observed in the gas-cooling-and-freezing experiments. The largest observed shell thickness and the measured fraction solid, assuming the liquid core to be an ellipsoid, are plotted in Figure 6 as a function of holding time at the solidification plateau, and compared to the calculated result. The observed solid shell thickness was larger than the calculated values at the beginning due to preferential cooling on the topside of the specimen caused by the flow of gas coolant. For this reason, the thickness at that location was larger than the values calculated by assuming spherical symmetry. The fraction solid increased with holding time at the solidification plateau. The good agreement between calculated and measured values shows that the heat transfer coefficient assumed in the calculation was reasonable.

Calculated cooling curves for the quenched specimen are shown in Figure 7. Heat was extracted very rapidly by quenching, so that thermal diffusion could not reach steady state during solidification. The cooling rate for both the gas-cooling experiments and the quenching experiments are plotted in Figure 8 as a function of position within the specimen. In the quenching experiments, the cooling rate increased sharply near the specimen surface. Thus, at a position 50 μm away from the surface, the cooling rate was larger than $1 \times 10^6 \text{ Ks}^{-1}$, whereas at $r \leq 2 \text{ mm}$ it was smaller than $5 \times 10^3 \text{ Ks}^{-1}$. In contrast, the cooling rate in the gas-cooling experiments was nearly uniform at around 50 Ks^{-1} throughout the entire specimen.

3. Microstructure and Microsegregation

a) Microstructure

Photomicrographs of the specimens were taken after electrolytic etching. The dendrite surface was stained dark because of solute microsegregation. The final grain boundary could also be seen as a sharp black line; however, it did not always represent the original grain boundaries that formed during solidification because the phase transformation from ferrite to austenite and then from austenite back to ferrite occurred during the solid state cooling. To identify the original as-solidified grains, a careful tracing of the dendritic structure had to be carried out, based on the individuality of dendrite orientation.

Figure 9 exhibits the microstructure of a high-Ti-alloy specimen melted in 4%N₂-gas. Columnar dendrites grew radially from the surface inward, while equiaxed dendrites formed in the last region to solidify. The secondary arm spacing of the columnar dendrites was typically 45 μm and did not appear to depend on alloy composition and location, which would indicate that the cooling rate in the gas-cooled specimen was nearly uniform, in agreement with calculations. The secondary arm spacing of the equiaxed dendrites was also similar to the spacing of the surrounding columnar dendrites. Most of the final grain boundaries followed the original grain boundaries, which meant that no noticeable grain boundary migration occurred presumably because of the presence of dispersed TiN particles which anchored grain boundaries.

Figure 10 shows photomicrographs of a low-Ti-alloy specimen melted in 4%N₂-gas. The high undercooling of 30 K experienced by that specimen is not evident in the microstructure shown in Figure 10. Dendrite grains that appear in a very small region near the shrinkage cavity may be equiaxed, formed by the gathering and growth of a number of dendrite fragments. They may also be columnar dendrites that grew quasi-perpendicular to the polished surface and, in cross-section, appears misleadingly to be equiaxed. Grain boundaries still roughly followed the original

grain structure, with a tendency to straighten out in order to reduce grain boundary area.

Figure 11 shows photomicrographs of a low-Ti-alloy specimen melted in no- N_2 -gas. The entire specimen had a columnar structure except near the topside surface, where a layer of a “spherical structure” consisting of spherical grains could be observed. This spherical structure indicates that this specimen had experienced some degree of undercooling, although the pyrometry did not detect any recalescence. The dendritic structure that had grown rapidly during recalescence partially remelted yielding a large number of fragments that spheroidized rapidly. The final grain boundaries no longer followed the original grain boundary position, and polygonal grains formed, instead.

Photomicrographs of a high-Ti-alloy specimen melted and gas-cooled in 4% N_2 -gas, and held for 3.5 s at the solidification plateau prior to quenching in liquid In-Ga are exhibited in Figure 12. Columnar dendrites are seen growing inward from the whole surface although the shell thickness was much larger on the topside. The core portion was still molten when the structure was frozen in In-Ga. The quenched liquid core led to a fine cellular structure with a shrinkage cavity. Several equiaxed dendrite grains can be seen as black spots in the frozen core. The secondary dendrite arms of the equiaxed grains are much finer than those of the fully developed columnar grains found in the gas-cooled specimens. This observation indicates that these equiaxed dendrite grains did not have sufficient time to coarsen after nucleation.

Figure 13 shows a high-Ti-alloy specimen melted and gas-cooled in 4% N_2 -gas, and then quenched in In-Ga after a 6.1 s holding at the solidification plateau. Comparison with the specimen of Figure 12 shows a larger fraction solid at a time of quench, due to the longer holding time, and equiaxed dendrite grains spread over a wider area in the frozen core region. Some of the equiaxed grains had coarser dendrite arms, as shown in the bottom photomicrograph. This indicates that those equiaxed grains had longer time to coarsen prior to quench.

Figure 14 shows a low-Ti-alloy specimen melted and gas-cooled in no-N₂-gas, and then quenched in In-Ga after holding for 3.7 s at the solidification plateau. The columnar dendrite shell did not cover the whole surface as it did in Figure 12. No equiaxed dendrites could be found in the quenched core region. These two differences were probably due to the presence or not of TiN particles. In the case of high-Ti-alloy melted in 4%N₂-gas, TiN formed both at the surface and the bulk of the specimen, and acted as a nucleation site during solidification. The particulate TiN layer on the specimen surface encouraged the columnar dendrite shell to cover the whole surface and TiN particles in the interior promoted nucleation of the equiaxed dendrite grains. In the case of low-Ti-alloy melted in no-N₂-gas, TiN did not form and the columnar dendrite shell covered only a part of the surface without formation of equiaxed dendrite grains in the specimen interior.

Figure 15 shows a high-Ti-alloy specimen melted in 4%N₂-gas and quenched in In-Ga. The specimen had a polar cap shape and an irregular surface on the top with flow lines appearing inside. This complicated shape was due to the fluid flow that occurred when the spherical liquid droplet impacted the quenching bath. The smoothly curved bottom surface solidified immediately after contact with In-Ga. In contrast, the upper region of the specimen did not solidify so rapidly, allowing the fluid to flow and the top surface to deform. The microstructure was predominantly cellular because of the high cooling rate and the large thermal gradient, except in the region within the flow lines, where a very fine dendritic structure could locally be detected. The typical cell spacing was approximately 6 μm at a position about 1.5 mm from the bottom surface. The structure became finer near the surface, because of the corresponding higher cooling rate, with a cell spacing of 1.5 μm at a position 200 μm from the surface and 0.65 μm at a position 50 μm from the surface.

Figure 16 shows a low-Ti-alloy specimen melted in no-N₂-gas and quenched in In-Ga. This specimen is similar to that of Figure 15. Both of them exhibit no equiaxed grains, albeit for different reasons. The specimen of Figure 16 does not

contain TiN particles. On the other hand, the specimen of Figure 15 contains either primary TiN particles which did not act as nucleants because of lack of time or secondary TiN particles.

Variation of the secondary dendrite spacing and cell spacing versus calculated cooling rate is shown in Figure 17. The experimentally determined relationship is described by the following equation:

$$d = 214\dot{T}^{-0.417} \quad (13)$$

where d is secondary dendrite arm spacing or cell spacing in μm and \dot{T} is calculated cooling rate in Ks^{-1} . The experimental relationship in low alloy steel measured by Suzuki, et al. [32], and that in stainless steel 440C measured by Brower [4] are also shown in the same figure. The relationship in this work is in good agreement with the result of Suzuki, et al., rather than the Brower's. This may be attributed to the fact that the stainless steel 440C, used in Brower's work, solidifies into austenite instead of ferrite as in the other two cases.

b) Microsegregation

Chromium and titanium microsegregation in the dendritic structure of a high-Ti-alloy specimen melted and gas-cooled in 4%N₂-gas and that in the cellular structure of a quenched specimen were evaluated by EPMA and are shown in Figure 18. Both the concentrations of chromium and titanium were higher near the dendrite or cell surface, and titanium segregation was more pronounced than that of chromium in both cooling processes. Since the beam spot size, 1 μm , was not small compared to the solidification structure especially in the quenched specimen and the calibration of EPMA for this particular composition was not carried out, the result should not be interpreted quantitatively.

c) Summary

From the specimen observation, the microstructural characteristics and their dependence on alloy composition may be summarized as follows:

- 1) The solidification structure in the gas-cooled specimens was dendritic. The solidification structure in the quenched specimens was cellular with a finer spacing near the quenched surface. Titanium was segregated to the interdendritic or intercellular spaces.
- 2) During gas-cooling of high-Ti-alloy specimens melted in 4%N₂-gas, the equiaxed dendrite grains grew and coarsened, and a columnar dendrite shell covered the whole surface at the early time of the solidification. By contrast, during gas-cooling of low-Ti-alloy specimens melted in either 4%N₂-gas or no-N₂-gas, few or no equiaxed dendrite grains formed and the columnar dendrite shell covered only a part of the surface.
- 3) Generally, the final grain boundaries followed the original as-solidified grain boundaries in high-Ti-alloy specimens melted and gas-cooled in 4%N₂-gas, while grain boundaries migrated and tended to form polygonal grains in other gas-cooled specimens.
- 4) No clear effect of TiN content could be found on the microstructure of quenched specimens.

4. Nonmetallic Inclusions

a) Morphology and Location

Figure 19 shows secondary electron images of TiN inclusions in high-Ti-alloy specimens melted and gas-cooled in 4%N₂-gas. Most inclusions were located along the interdendritic spaces. Because of their cubic crystalline structure, TiN particles typically exhibited cuboidal shapes, which appeared polygonal in a polished section. However, inclusions with various other shapes were also observed, as shown in Figure 19. Those included a “dog-bone-like” particle (A), a coalescent particle (B), a

cuboidal particle with a rod at its corner (C), agglomerated cuboidal particles (D), a cuboidal particle showing terraces on its face (E), and strings of irregular “worm-like” particles (F).

Figure 20 shows secondary electron images of TiN inclusions in high-Ti-alloy specimens melted in 4%N₂-gas and quenched in In-Ga. The majority of inclusions were cuboidal and located along the intercellular spaces. Due to the higher cooling rate, they were smaller than those found in the gas-cooled specimens. Irregularly shaped particles were found as shown in (C) and (D); however, their shapes were relatively simple and agglomerates were absent. Grain boundaries are also favored sites for the presence of inclusion particles. However, it is not clear whether the inclusions formed along the intercellular boundaries which subsequently became the final grain boundaries, or resulted from solid state precipitation that occurred preferentially along grain boundaries.

In both gas-cooled and quenched specimens, most of the inclusions were located in the interdendritic or intercellular spaces and the probability of finding irregular particles was higher in those regions. This accumulation of inclusions was presumably due to microsegregation of titanium and nitrogen. The concentration product [Ti][N] was larger in the interdendritic or intercellular spaces than within the dendrite arms or cells; therefore, TiN formation occurred easily at the interdendritic region. If the supersaturation of [Ti][N] was very high, a number of cuboidal particles could nucleate and grow in a small region, leading to the agglomerates or string of particles. It is also possible that the crystallographic law for cuboidal growth was broken and the particles grew preferentially along the interdendritic or intercellular spaces. The accumulation of inclusions in interdendritic or intercellular spaces may also be attributed to the pushing of particles by the advancing solidification front as opposed to engulfment by the solid. It may occur when the energy of the interface particle/solid is higher than that of the interface particle/liquid [33] or when particles have a lower thermal conductivity than the matrix [34]. Comparison of the inclusion

size observed in the present work and the experimentally determined critical size in a literature [35] to be captured by advancing solidification front is shown in Appendix C.

b) Composition

Figure 21 shows an example of EDS spectrum from a cuboidal particle (edge length of 2 μm) in a high-Ti-alloy specimen melted and gas-cooled in 4% N_2 -gas. Titanium could be easily found by its K_α peak at 4.508 keV. EPMA concentration images of iron, titanium and nitrogen for a large quadrangular inclusion (edge length of 10 μm) in a high-Ti-alloy specimen melted and gas-cooled in 4% N_2 -gas are shown in Figure 22 along with the backscattered electron image. These images show that the inclusion contained high concentrations of titanium and nitrogen and was depleted in iron. Aluminum and manganese were also analyzed; however, their concentrations in the inclusion were indistinguishable from the surrounding matrix. Point analyses were also carried out for the small inclusions in the quenched specimens (edge length of 0.1 to 0.3 μm). Only titanium and nitrogen could be detected, while aluminum, manganese, sulfur and carbon were indistinguishable from the background level.

In any analyses by EDS and EPMA, elements other than titanium and nitrogen could not be detected. However, solid state precipitation of other inclusions such as manganese sulfide (MnS), titanium carbide (TiC) and titanium carbosulfide ($\text{Ti}_4\text{C}_2\text{S}_2$) is also thermodynamically possible in these alloy systems [36]. Such inclusions presumably did not grow to larger sizes, beyond the SEM resolution limit because of the high cooling rate and the low solute diffusivity in the solid state. These solid state precipitates may be revealed using the extraction-replica technique and transmission electron microscopy (TEM).

c) Size and Amount

Measurements of inclusion size were carried out for specimens processed under different conditions in order to establish its dependence on alloy composition and cooling rate. Furthermore, the size of inclusions in the frozen core region of gas-cooled-and-frozen specimens was also measured in order to determine the kinetics of primary inclusion formation.

Figure 23 shows the inclusion size distribution of the specimen of Figure 9, a high-Ti-alloy specimen melted and gas-cooled in 4%N₂-gas. The particle size varied in a wide range from 0.15 to 10 μm. The average size of all inclusions, observed by both SEM and optical microscopy was 0.382 μm. Assuming all the inclusions to be TiN, the nitrogen concentration, [N], contained in TiN was calculated from the area fraction of particles and found to be 0.0273 wt%. The cuboidal particles, from which the size distribution was determined, comprised 68 % of the total amount (0.0187 wt%[N]). The majority of other irregular particles had “worm-like” shapes forming strings along the interdendritic spaces.

Figure 24 shows the inclusion size distribution of the specimen of Figure 10, a low-Ti-alloy specimen melted and gas-cooled in 4%N₂-gas. The particle size varied in a range from 0.25 to 4 μm. The distribution of inclusions smaller than 1 μm was similar to that of the high-Ti-alloy specimen even though the absolute number density of inclusions was smaller in this case. This suggested that the size distribution for inclusions smaller than 1 μm was independent of the degree of solute supersaturation in the gas-cooled specimens. The largest inclusion size observed was 4 μm, which is smaller than that of the high-Ti-alloy specimen. Such large particles were presumably primary inclusions, although the required solute supersaturation could not occur at the liquidus temperature with this low titanium content. The formation of such large inclusions could be attributed to the supersaturation only if the specimen was undercooled. In this case, particles that formed in the undercooled liquid and triggered the recalescence event and then were trapped in the solid without remelting in the

liquid. [N] contained in TiN was 0.0068 wt% and the cuboidal particles comprised 62 % of that value (0.0042 wt%[N]). This ratio is also similar to that of a high-Ti-alloy specimen, indicating that the morphology of inclusion particles, as well as the size distribution, is independent of the titanium concentration in the melt.

Figure 25 shows the inclusion size distribution of the specimen of Figure 15, a high-Ti-alloy specimen melted in 4%N₂-gas and quenched in In-Ga. The top figure shows the inclusion size distribution in the bulk of the specimen, 1 to 2 mm from the bottom surface, and the bottom figure shows that in the subsurface, around 200 μm from the bottom surface. In the interior bulk of the specimen, the particle size ranged from 0.09 to 0.32 μm with an average of 0.169 μm. [N] contained in TiN was 0.0183 wt% and the cuboidal particles comprised 50 % of that value (0.0091 wt%[N]). In the subsurface, the particle size was smaller, ranging from 0.05 to 0.14 μm with an average of 0.083 μm. [N] contained in TiN was 0.0092 wt% and the cuboidal particles made up 93 % of the total (0.0086 wt%[N]). This strongly suggests that the inclusion size decreases with increasing cooling rate. The absolute amount of cuboidal particles appears to be independent of cooling rate; therefore, the decrease in the total amount of TiN with increasing cooling rate can be attributed to the decrease in the amount of irregularly shaped particles.

To verify the assumption that all inclusions were TiN and also the accuracy of the measurement, the amount of [N] contained in TiN in specimens melted in 4%N₂-gas measured by microscopy is compared to that measured by wet chemical analysis in Figure 26. In wet chemical analysis, [N] contained in TiN was calculated from analyzed insoluble [Ti], assuming a stoichiometric ratio of 1:1. The values in both the high-Ti-alloy and the low-Ti-alloy specimens in the gas-cooled or gas-cooled-and-frozen condition appear to be in good agreement. Since the total amount of nitrogen was analyzed to be 0.020 to 0.023 wt%, as shown in Figure 4, most of the total nitrogen in the high-Ti-alloy specimens is contained in TiN. In contrast, in the low-Ti-alloy specimens only a half or less of the total nitrogen is contained in TiN. This

difference maybe attributed to the solubility of TiN in the solid state. Similarly to the solubility in the liquid iron, the concentration product of nitrogen and titanium in solid solution has a certain solubility limit; therefore, the higher titanium concentration in the high-Ti-alloy specimens leads to the lower nitrogen concentration in solid solution. In the case of the high-Ti-alloy specimen quenched in In-Ga, the microscopic measurement of [N] contained in TiN, led to a larger value relative to the wet chemical analysis. This may be attributed to an etching effect raising the apparent number density of TiN particles.

Figure 27 shows variation of the average inclusion size with calculated cooling rate for high-Ti-alloy specimens melted in 4%N₂-gas. The experimentally determined relationship is described by the following equation:

$$\bar{a} = 0.80\dot{T}^{-0.190} \quad (14)$$

where \bar{a} is the average inclusion size in μm and \dot{T} is the calculated cooling rate in Ks^{-1} . Since the primary inclusions were large in size but very small in number, the average inclusion size was primarily defined by the secondary inclusions. Brower's results [4] for SiO₂ inclusions in Fe-0.05wt%Si alloy are also plotted on the same figure. The dependence of the inclusion size on cooling rate is weaker in this work, probably because the amount of inclusions was relatively small and TiN formed as a solid phase in this work while the large amount of spherical SiO₂ inclusions formed as a liquid phase in Brower's.

To investigate the growth of primary inclusions, observations were carried out on large inclusions in the frozen core region of high-Ti-alloy specimens melted and gas-cooled in 4%N₂-gas and then quenched in In-Ga after holding for various times at the solidification plateau. The size distributions of inclusions larger than 1 μm observed by optical microscopy are shown in Figure 28. Considering the fact that the largest inclusion found in quenched specimens was 0.32 μm in size, inclusions larger than 1 μm could not possibly form during quenching, but instead existed beforehand.

Both the amount of [N] contained in those primary TiN inclusions larger than 1 μm , and the largest inclusion size are plotted versus holding time at the solidification plateau in Figure 29. The amount of primary inclusions began to increase after around 1 s of incubation time and their precipitation continued until equilibrium was achieved in the gas-cooled specimen, which solidified in about 9 s at the solidification plateau. Similarly, the largest inclusion size increased with holding time, exceeding 10 μm at the end.

d) Summary

The results of inclusion observation may be summarized as follows:

- 1) Most of the nitrogen in the high-Ti-alloy specimens and a half or less of the nitrogen in the low-Ti-alloy specimens are contained in TiN inclusions. The inclusions were mostly located along the interdendritic or intercellular spaces and had cuboidal shapes. However, irregularly shaped inclusions were also observed. Only titanium and nitrogen could be detected in the inclusions.
- 2) In the gas-cooled specimens, the inclusion size had a broad distribution, from 0.15 to 10 μm that was independent of the alloy composition. In the quenched specimen, the inclusion size ranged from 0.05 to 0.32 μm , becoming finer near the surface. The average inclusion size varies proportionally to $\dot{T}^{-0.190}$.
- 3) Inclusions larger than 1 μm observed in the quenched core of the gas-cooled-and-frozen specimens are of primary nature. These inclusions grew in size and in number density with holding time at the solidification plateau.

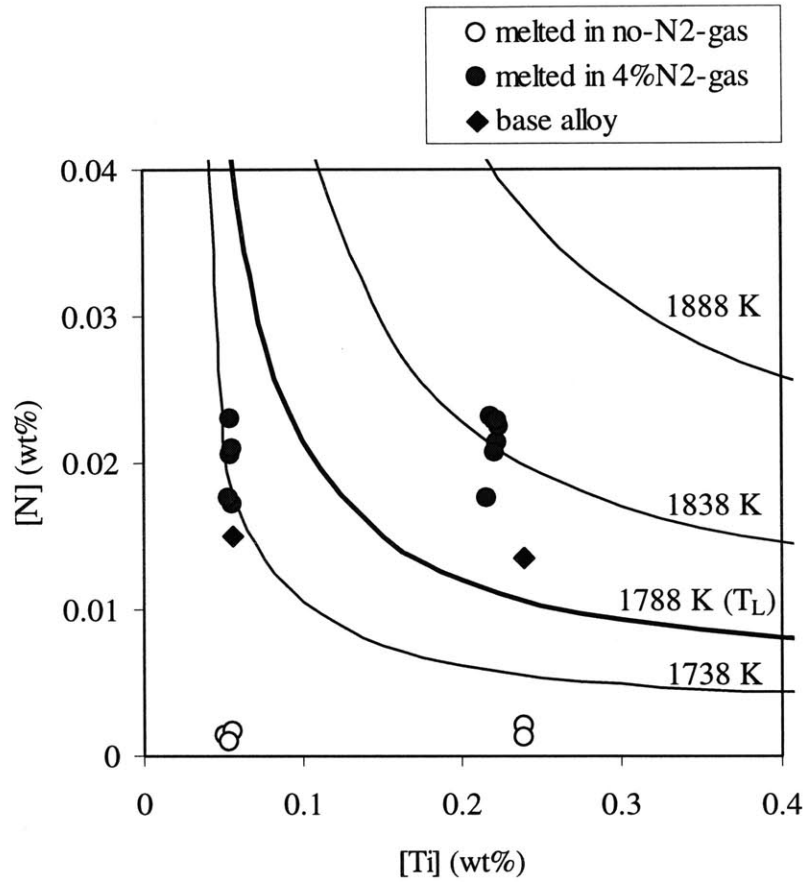


Figure 4 – Measured [Ti] and [N] in gas-cooled specimens and theoretical TiN solubility

Table 5 – Interaction coefficients
used in the calculation of TiN solubility [31]

$\epsilon_{ij}(I \rightarrow)$	Ti	N
C		0.13
Si	2.1	0.048
Mn	-0.43	-0.02
P	-0.06	0.059
S	-0.27	0.007
Cr		-0.0498
Cr ⁽²⁾ *		0.00034
Ti	0.006	-0.7379
Al		0.01
N	-2.536	0
O	-3.4	-0.12

*: coefficient for $[\text{Cr}]^2$

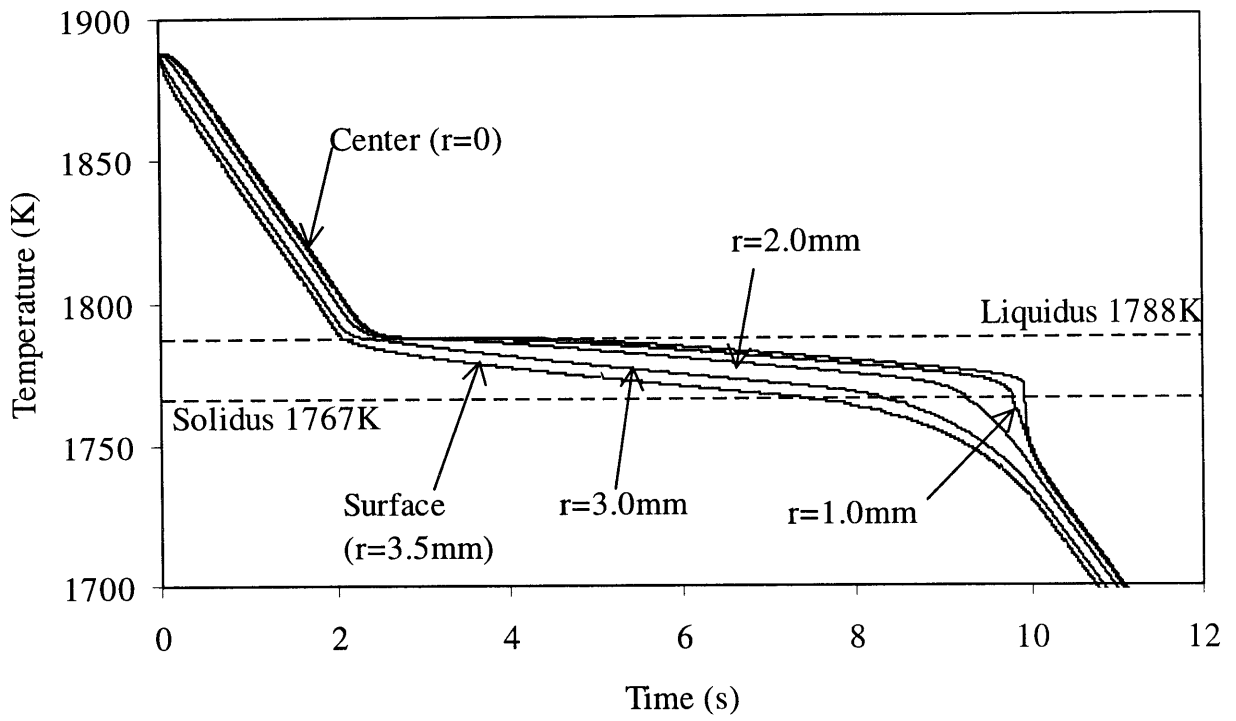


Figure 5 – Numerically calculated thermal history for a gas-cooled specimen

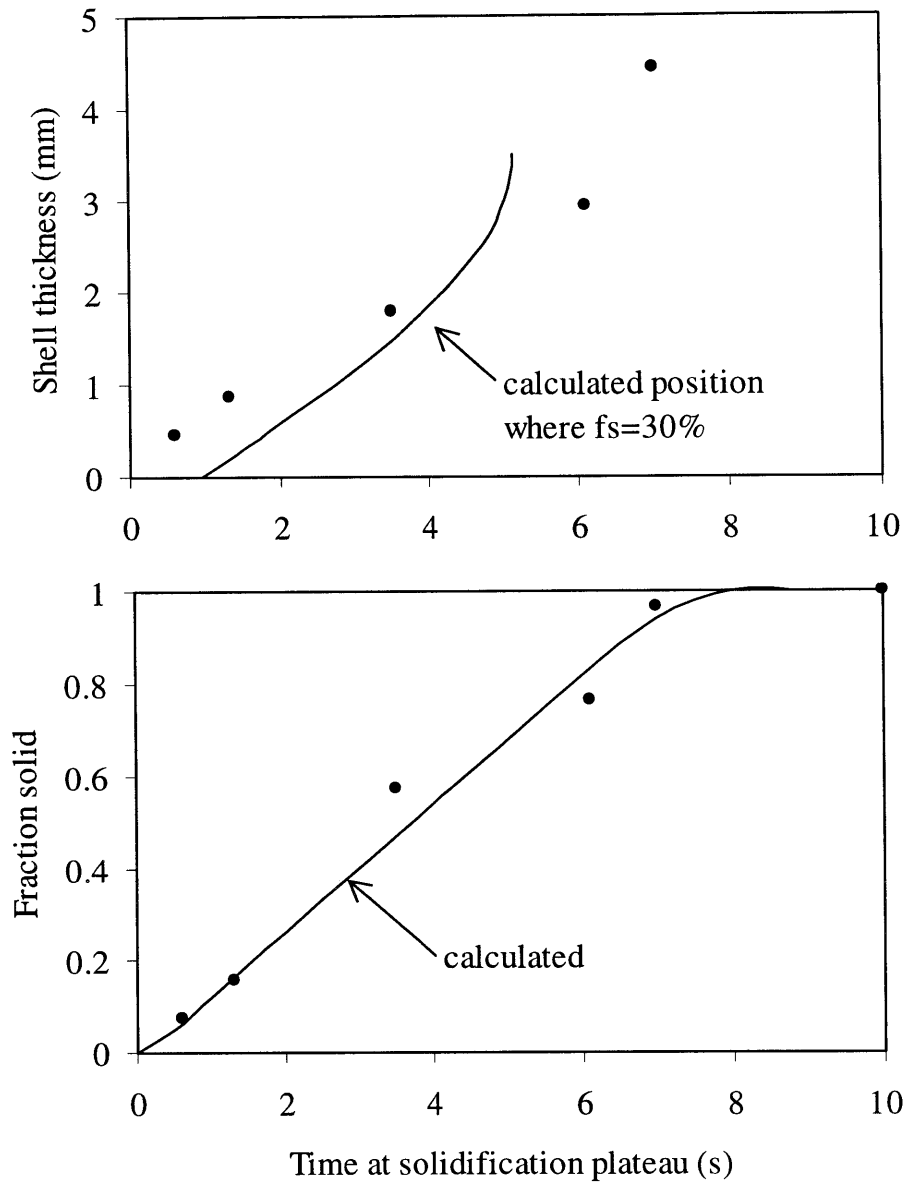


Figure 6 –Shell thickness and fraction solid as a function of time at solidification plateau for gas-cooling-and-freezing experiments and calculation

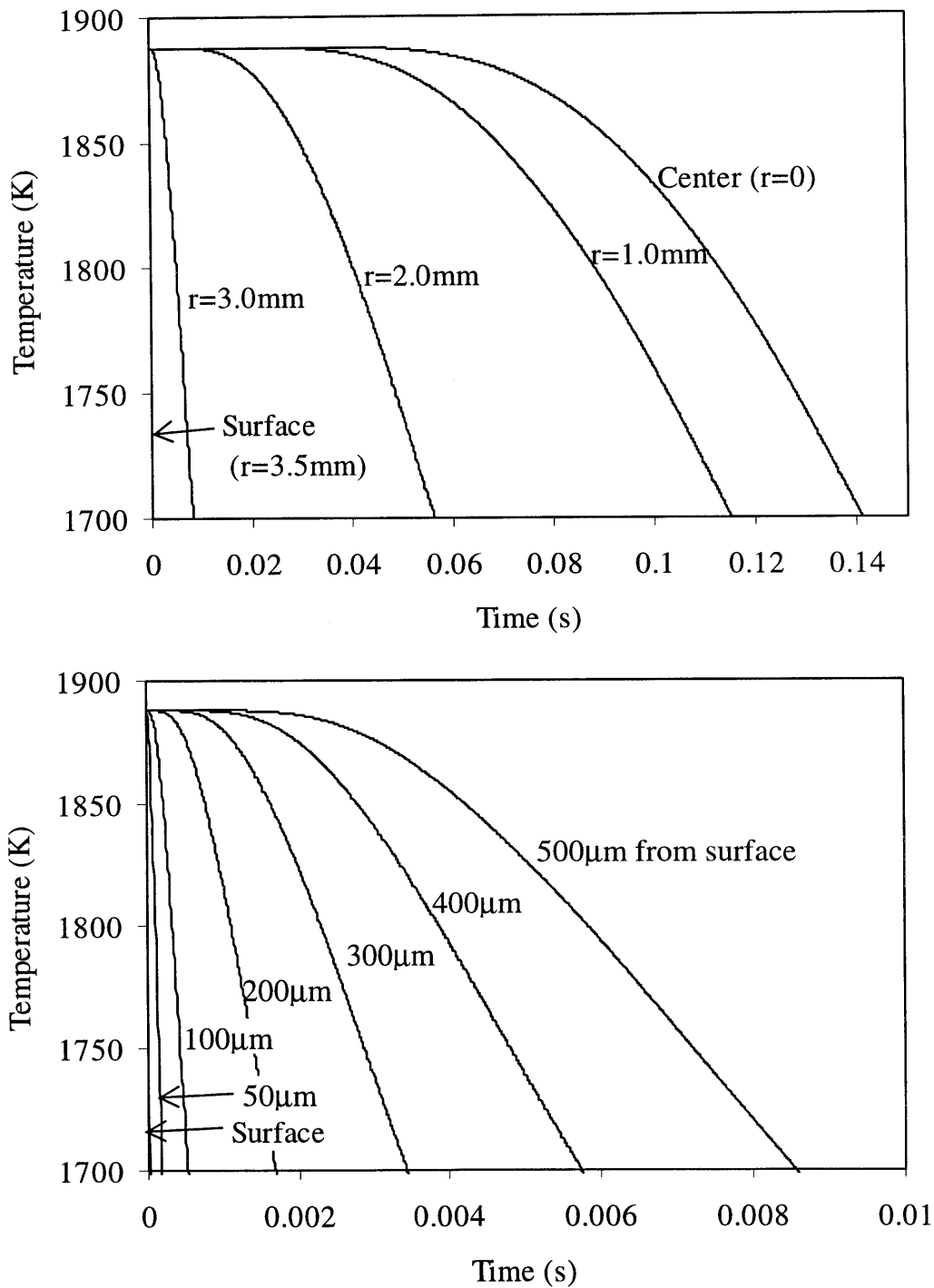


Figure 7 – Numerically calculated thermal history for a quenched specimen: in the bulk specimen as a function of radial distance from the surface (top), near the bottom of the specimen as a function of distance from the surface (bottom)

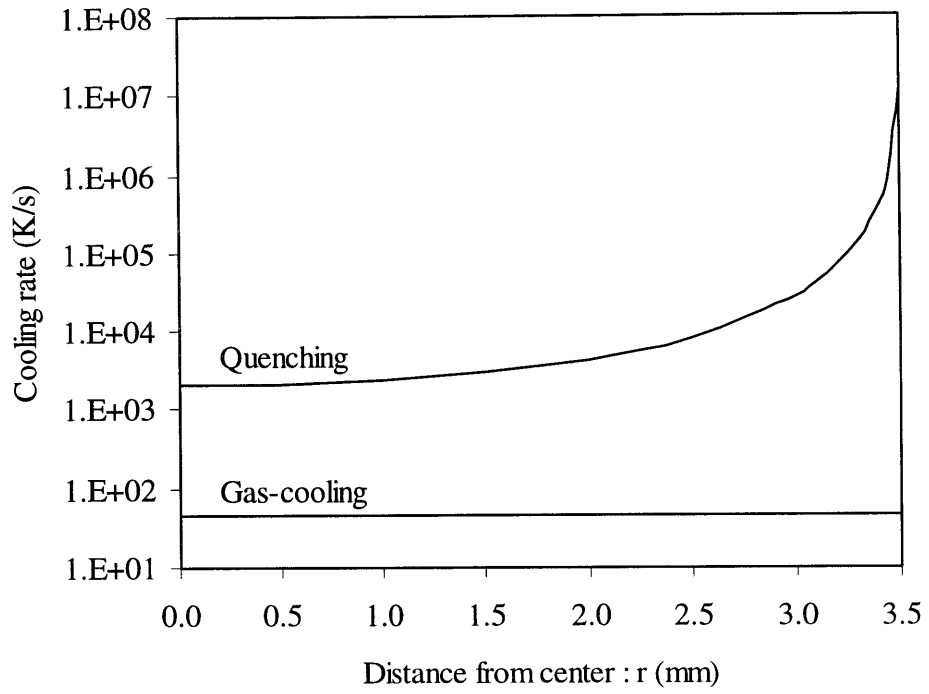
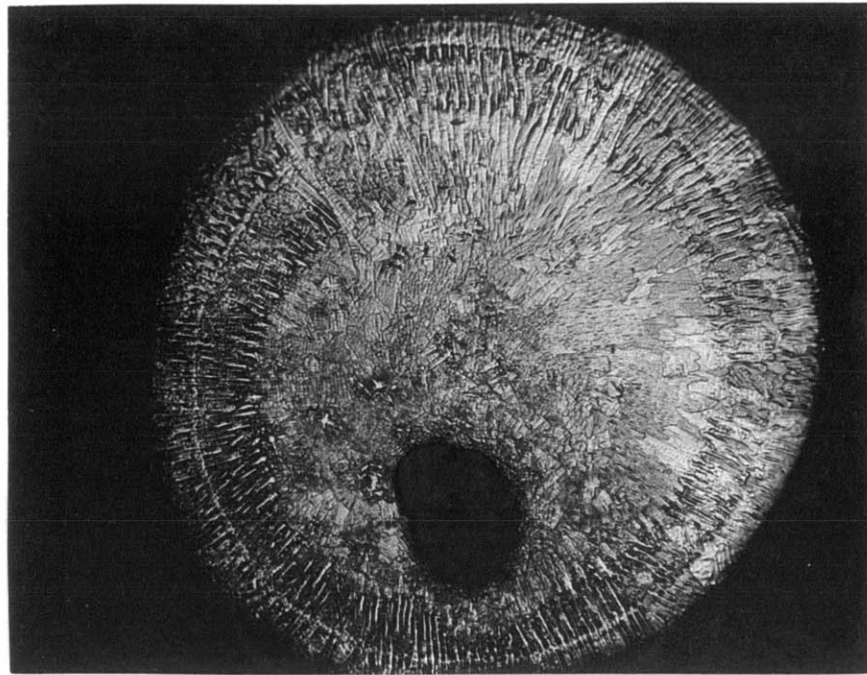
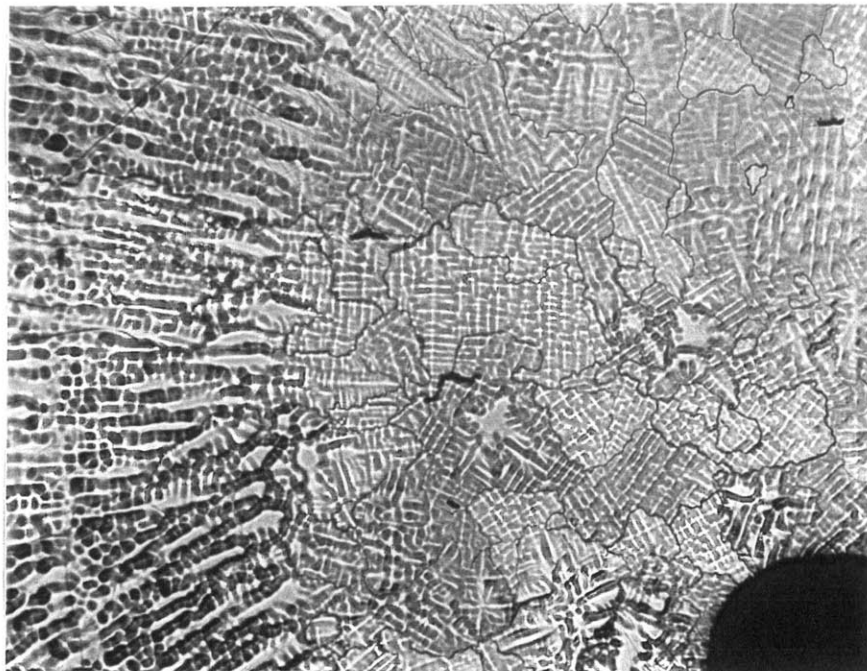


Figure 8 – Calculated cooling rate between 1863K and 1813K in a gas-cooled specimen and a quenched specimen

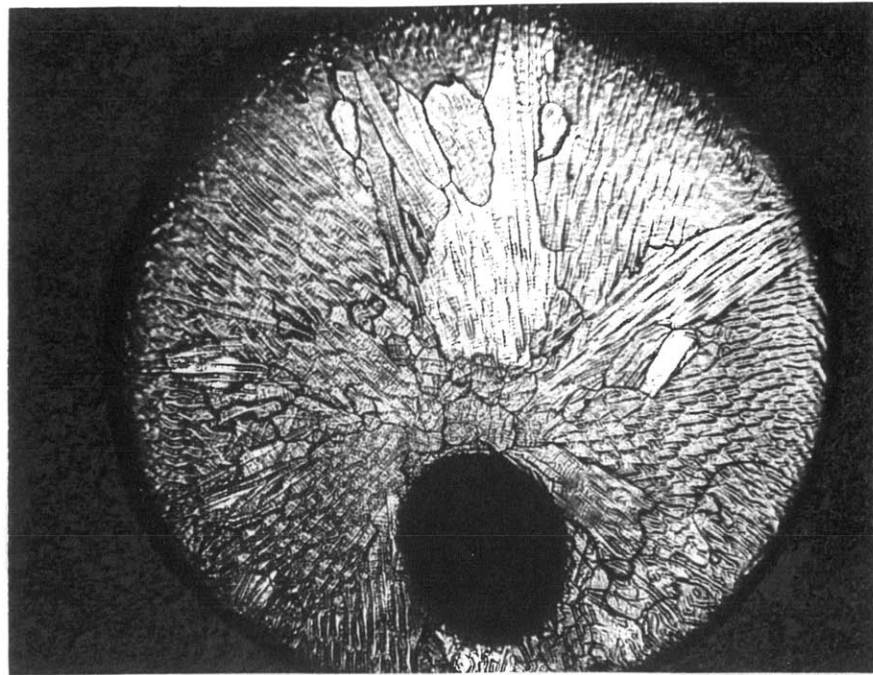


15× 1mm

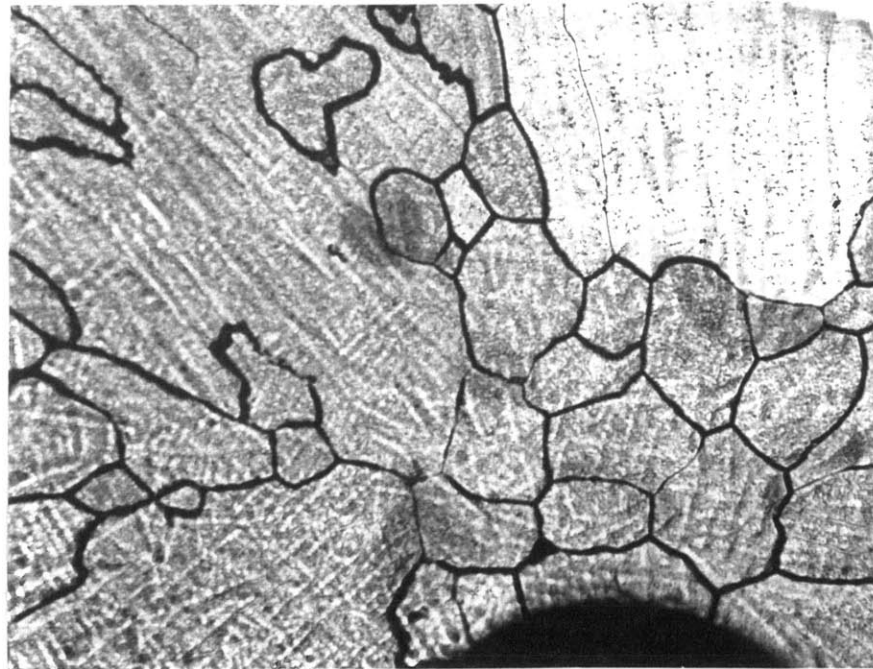


50× 300μm

Figure 9 – Microstructure of a high-Ti-alloy specimen melted and gas-cooled in 4%N₂-gas: the entire specimen (top) and the last portion to solidify (bottom)

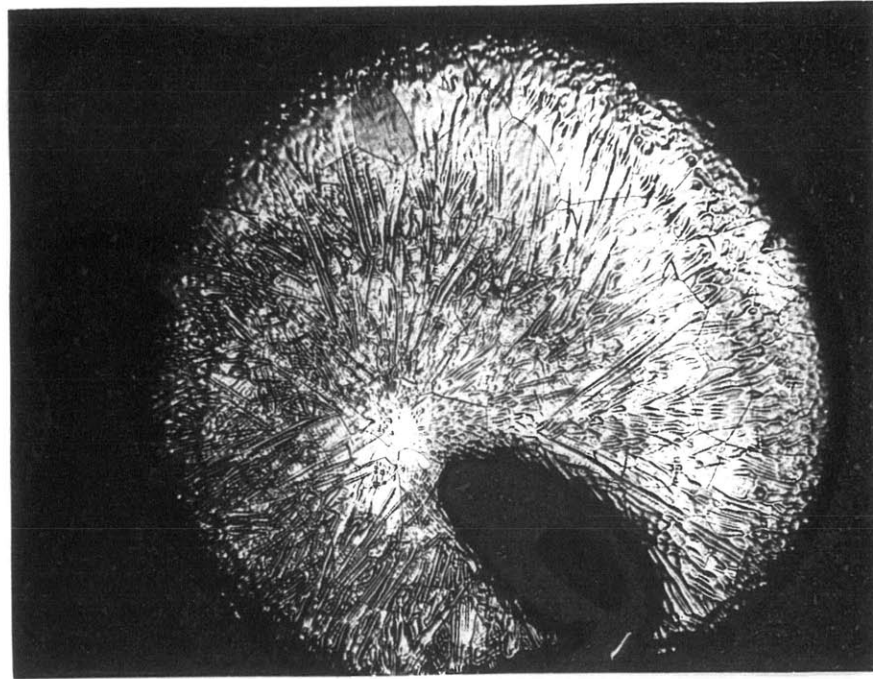


15× 1mm

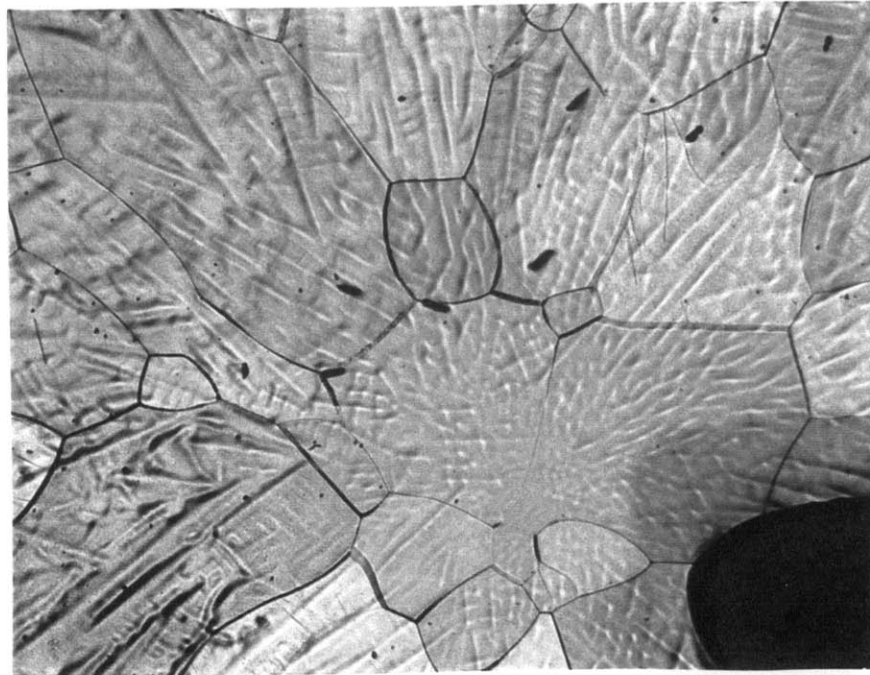


50× 300μm

Figure 10 – Microstructure of a low-Ti-alloy specimen melted and gas-cooled in 4%N₂-gas: the entire specimen (top) and the last portion to solidify (bottom)

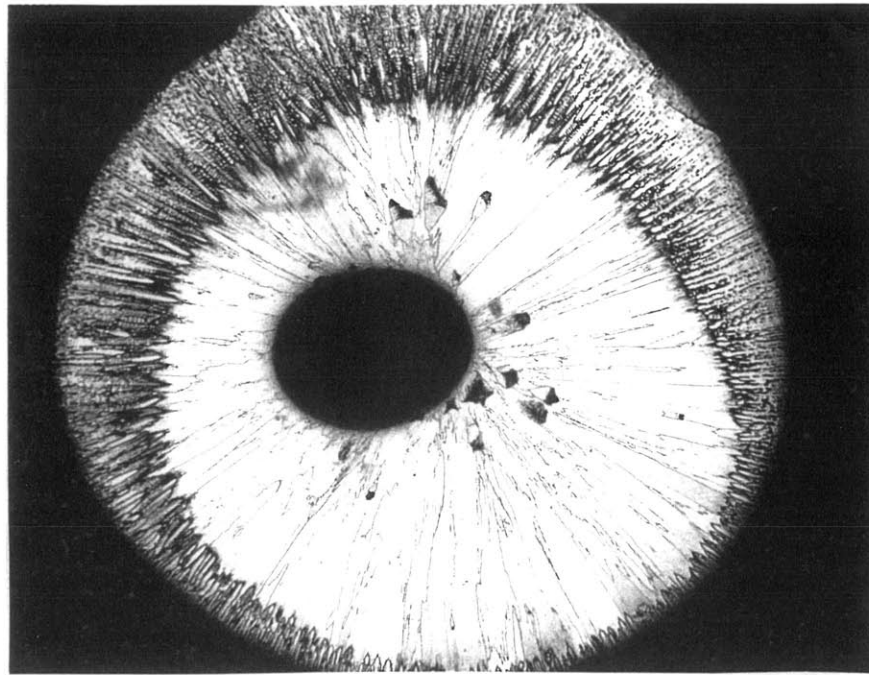


15× 1mm



50× 300μm

Figure 11 – Microstructure of a low-Ti-alloy specimen melted and gas-cooled in no-N₂-gas: the entire specimen (top) and the last portion to solidify (bottom)

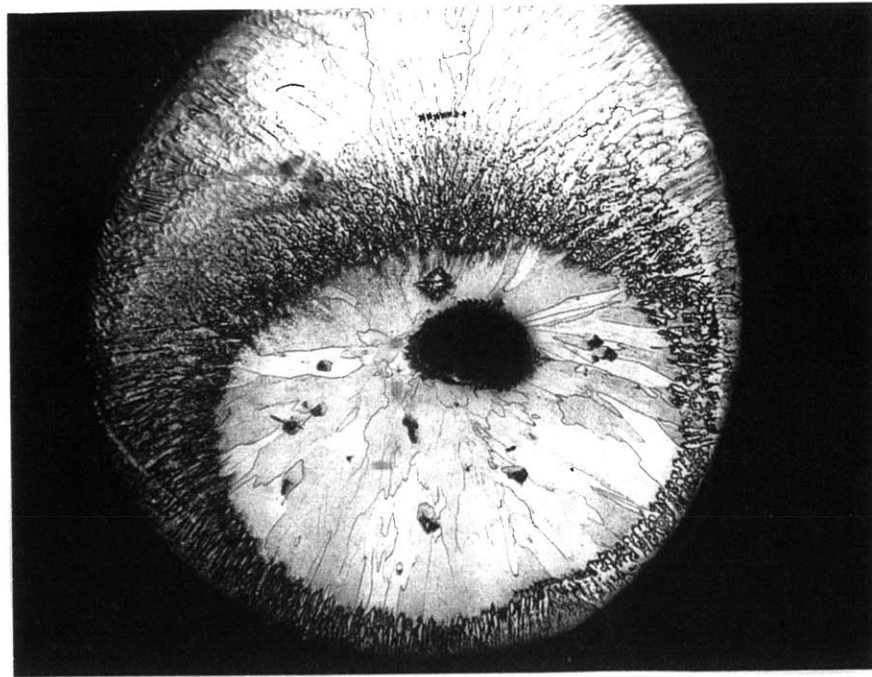


15× 1mm

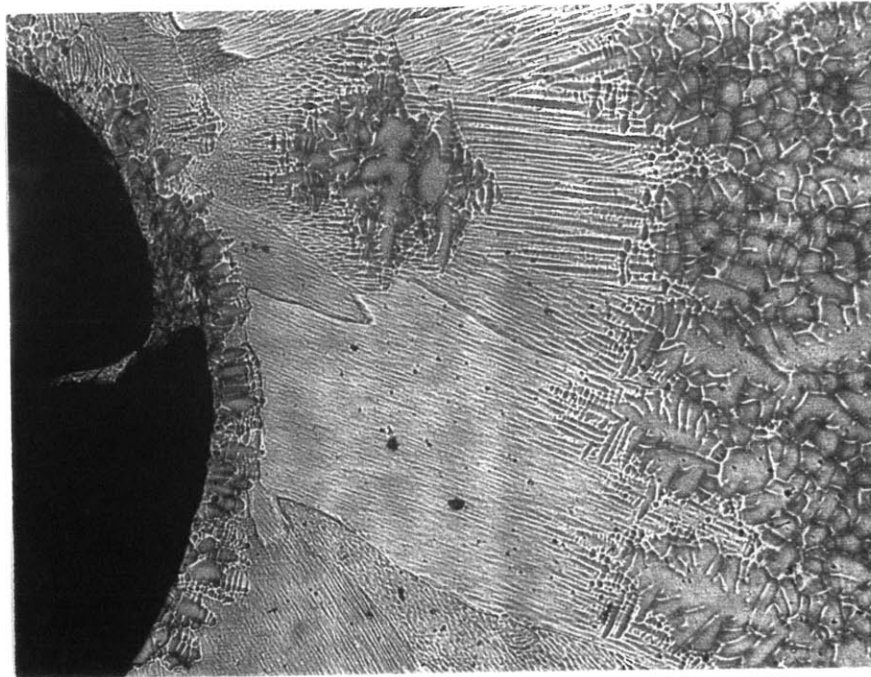


100× 150μm

Figure 12 – Microstructure of a high-Ti-alloy specimen melted and gas-cooled in 4%N₂-gas and then quenched in In-Ga bath after holding at the solidification plateau for 3.5 s: the entire specimen (top) and equiaxed dendrite grains in the frozen core (bottom).



15x 1mm



100x 150μm

Figure 13 – Microstructure of a high-Ti-alloy specimen melted and gas-cooled in 4%N₂-gas and then quenched in In-Ga bath after holding at the solidification plateau for 6.1 s: the entire specimen (top) and an equiaxed dendrite grain in the frozen core (bottom)

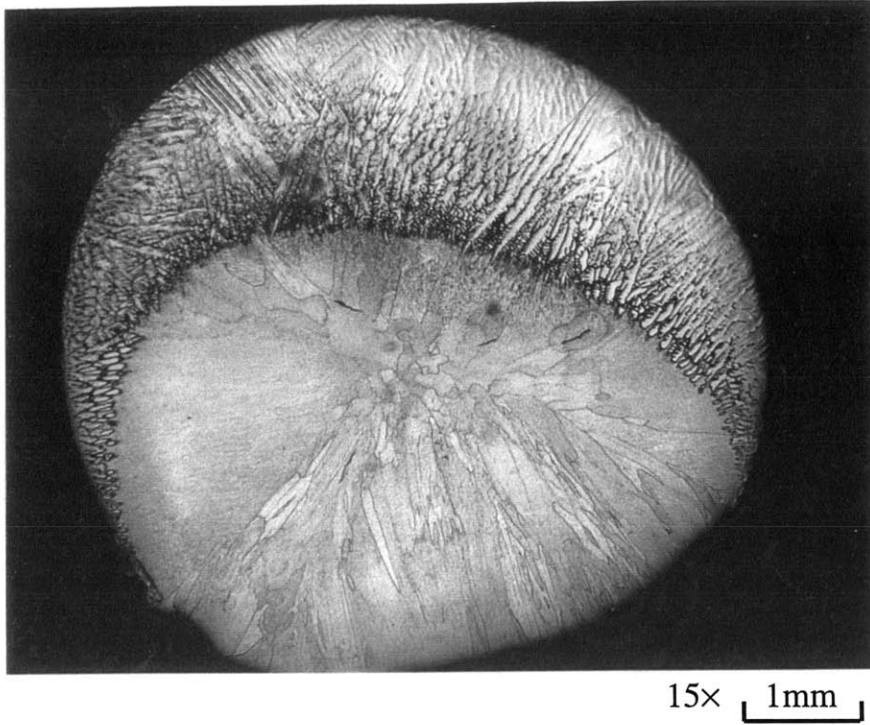
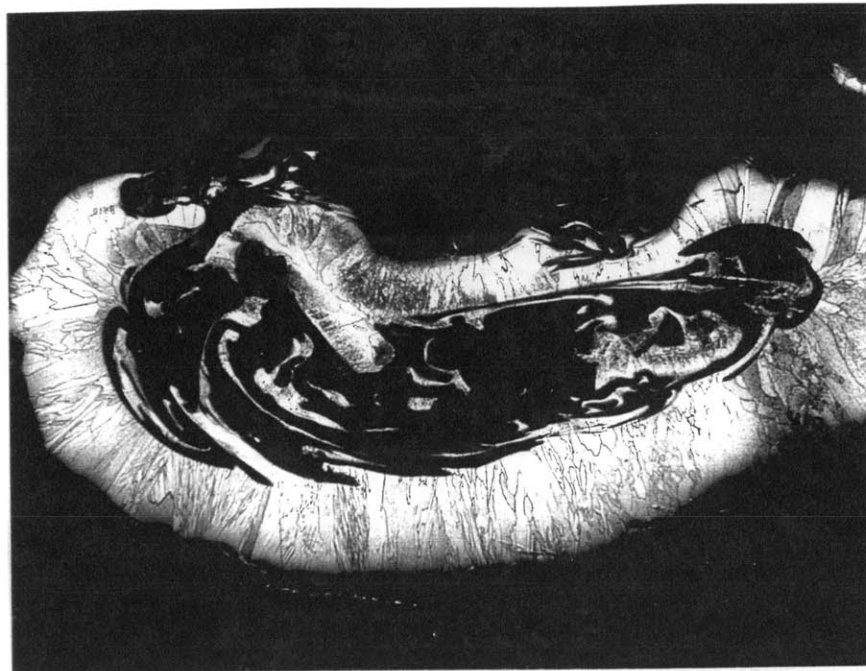
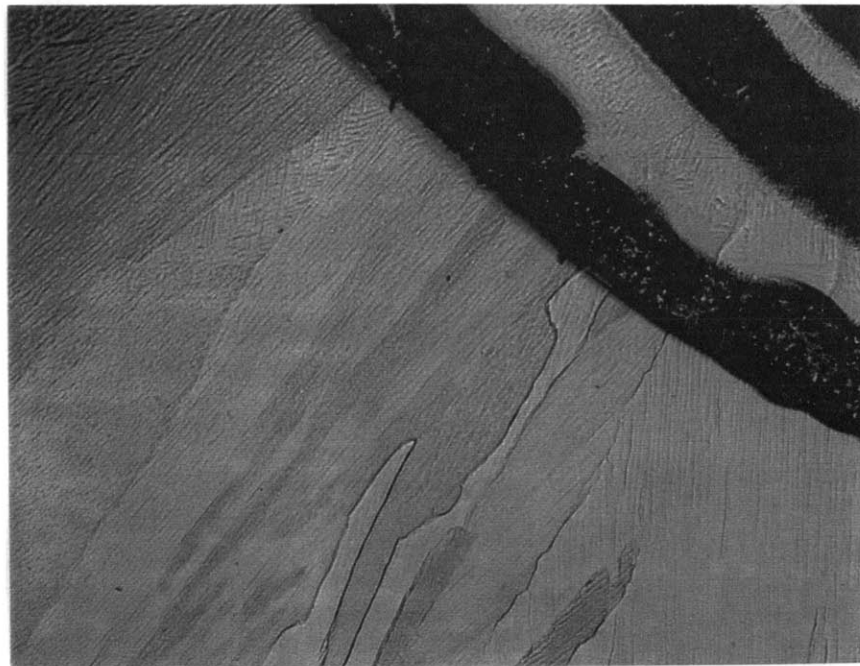


Figure 14 – Microstructure of a low-Ti-alloy specimen melted and gas-cooled in 4%N₂-gas and then quenched in In-Ga bath after holding at the solidification plateau for 3.7 s



15× 1mm



200× 100μm

Figure 15 – Microstructure of a high-Ti-alloy specimen melted in 4%N₂-gas and quenched in In-Ga bath: the entire specimen (top) and a portion near flow lines (bottom)

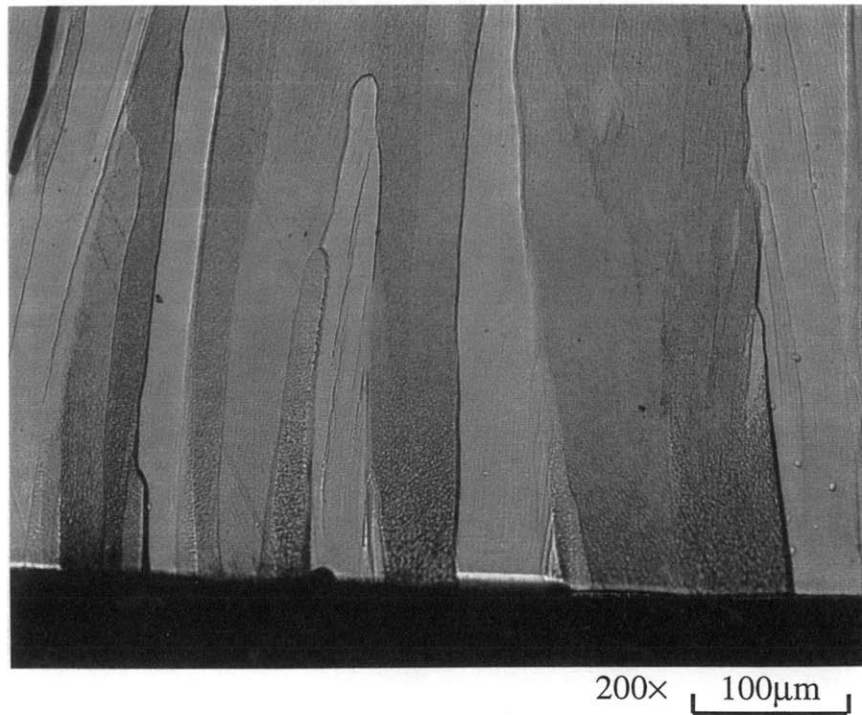
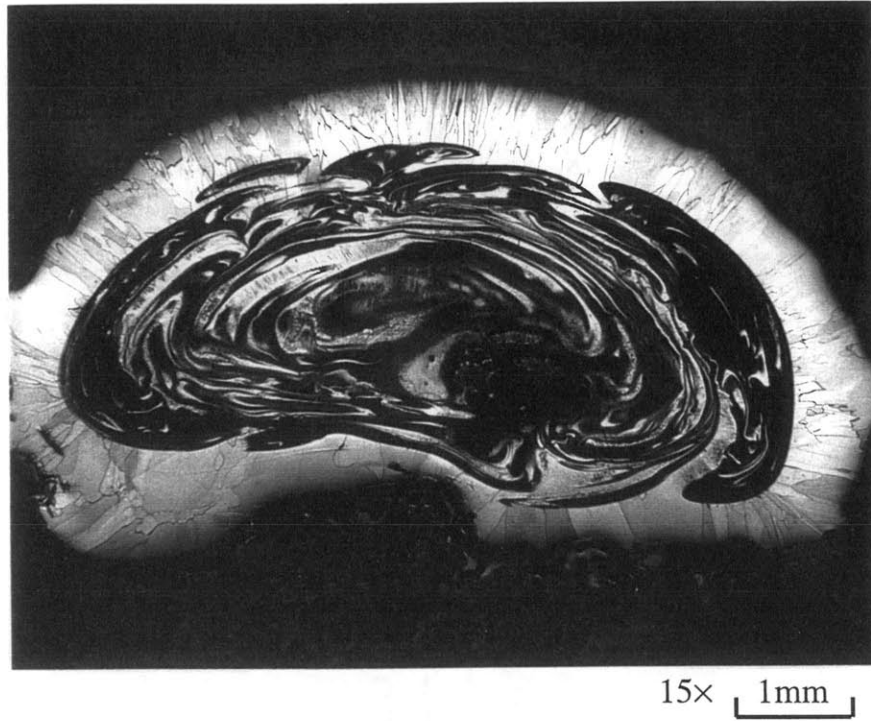


Figure 16 – Microstructure of a low-Ti-alloy specimen melted in no-N₂-gas and quenched in In-Ga bath: the entire specimen (top) and a portion near the bottom surface (bottom)

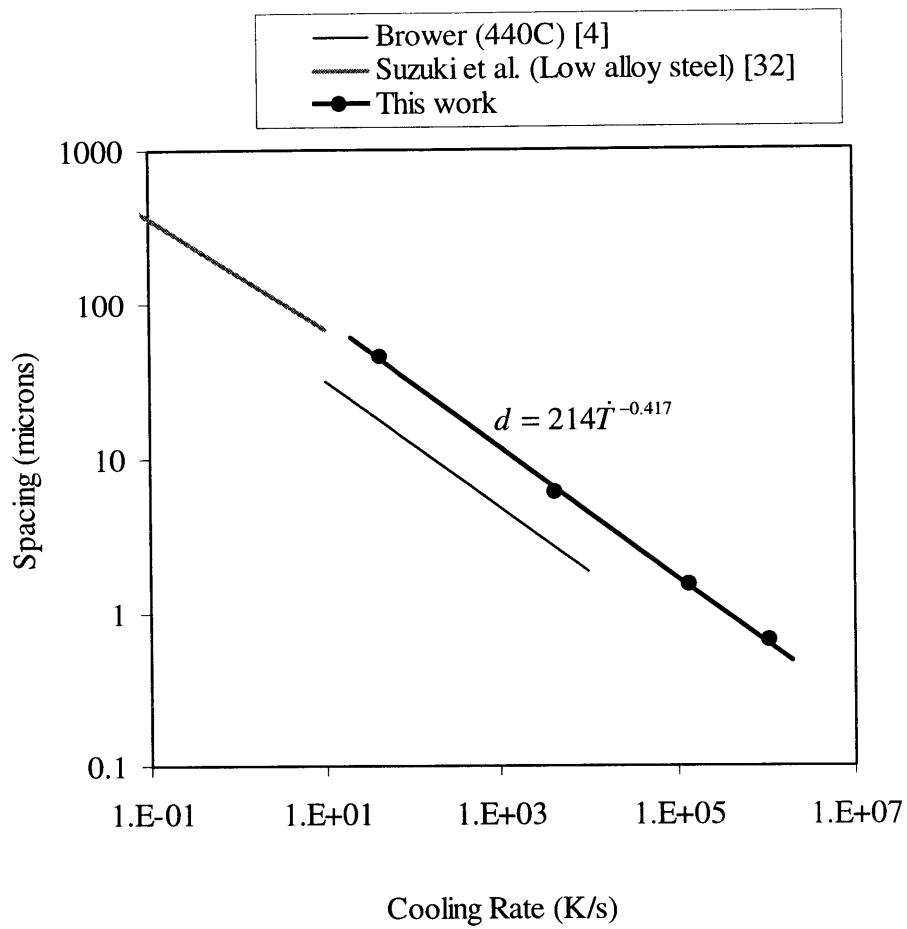


Figure 17 – Variation of secondary dendrite arm spacing and cell spacing with cooling rate

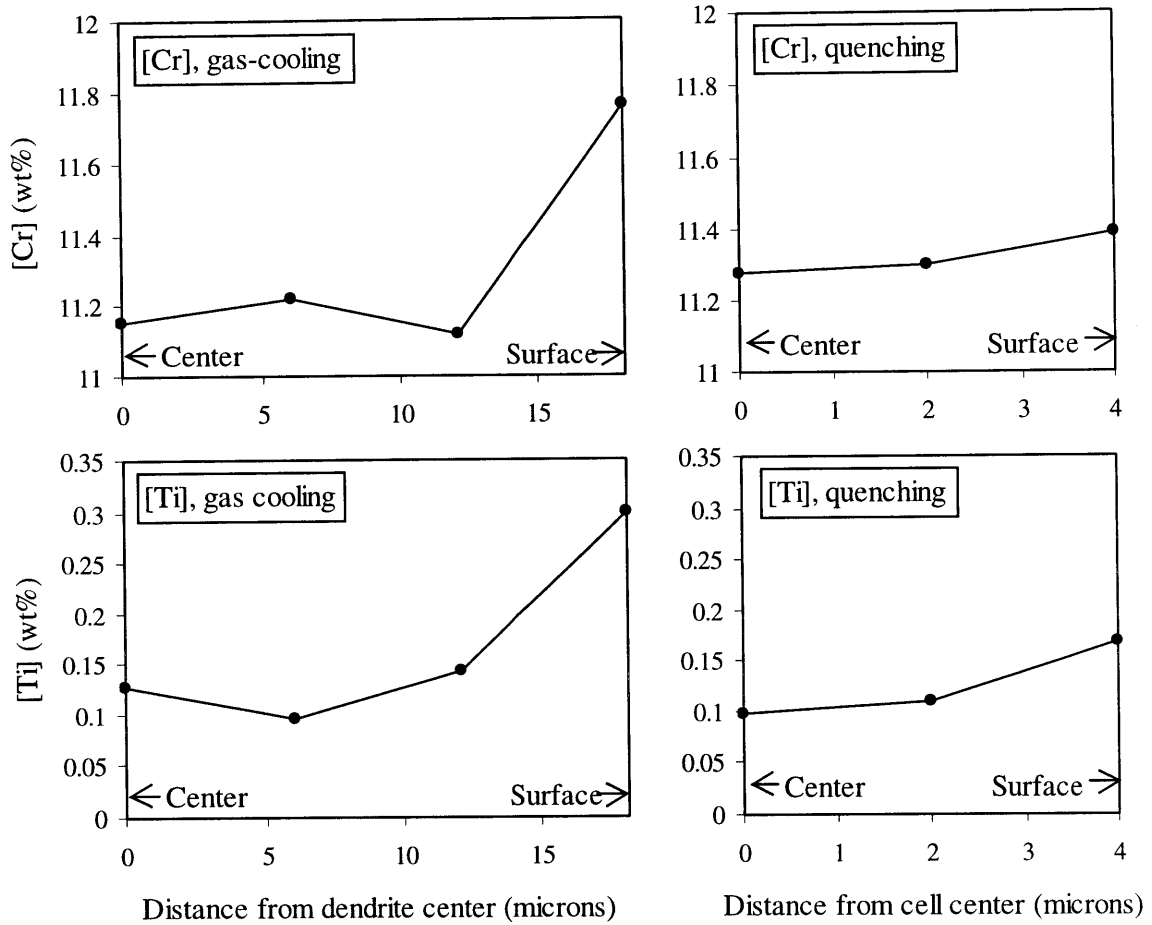


Figure 18 – Chromium and titanium microsegregation in high-Ti-alloy specimens melted in 4%N₂-gas: a gas-cooled specimen (left) and a quenched specimen (right)

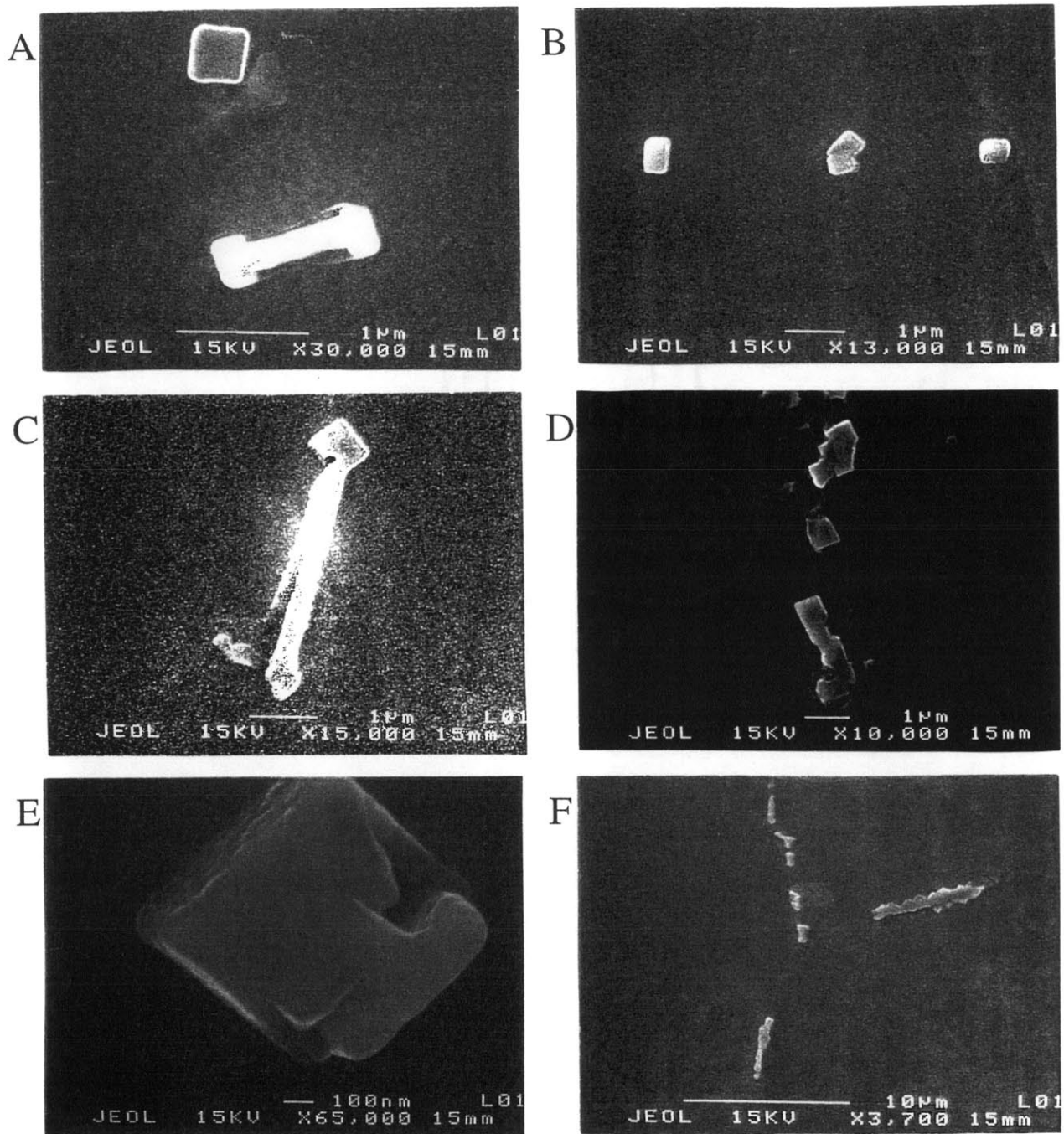


Figure 19 – SEM secondary electron images of inclusions in a high-Ti-alloy specimen melted and gas-cooled in 4%N₂-gas:

- [A]: a typical cuboidal particle (top) and a “dog-bone-like” particle (bottom)
- [B]: typical cuboidal particles and a coalescent particle (middle)
- [C]: a cuboidal particle with a rod at its corner
- [D]: agglomerated cuboidal particles
- [E]: a cuboidal particle showing terraces on its face
- [F]: strings of irregular “worm-like” particles along grain boundaries

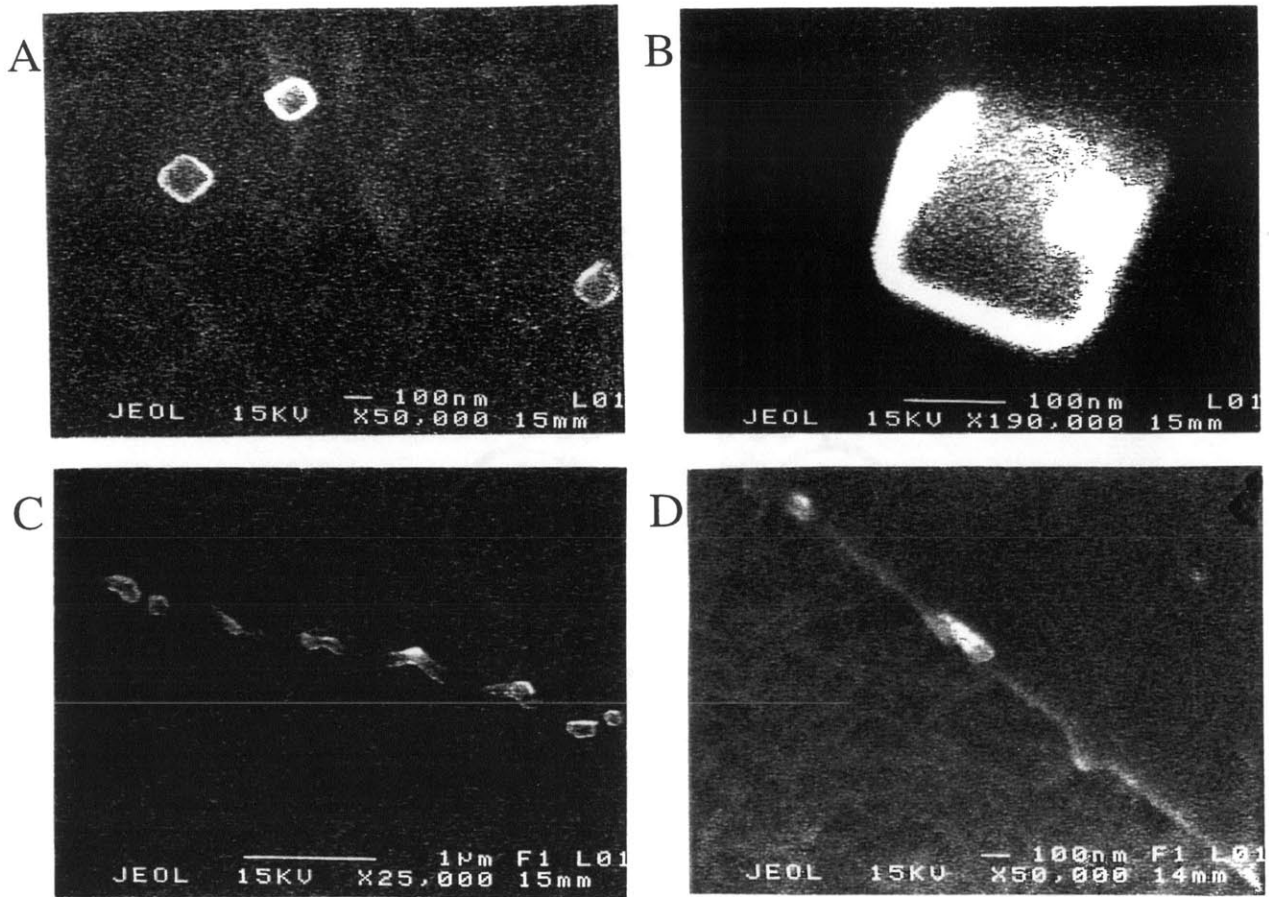


Figure 20 – SEM secondary electron images of inclusions in a high-Ti-alloy specimen melted in 4%N₂-gas and quenched in In-Ga bath:

[A][B]: typical cuboidal particles

[C]: a string of irregular particles along an intercellular space

[D]: fine irregular particles along a grain boundary

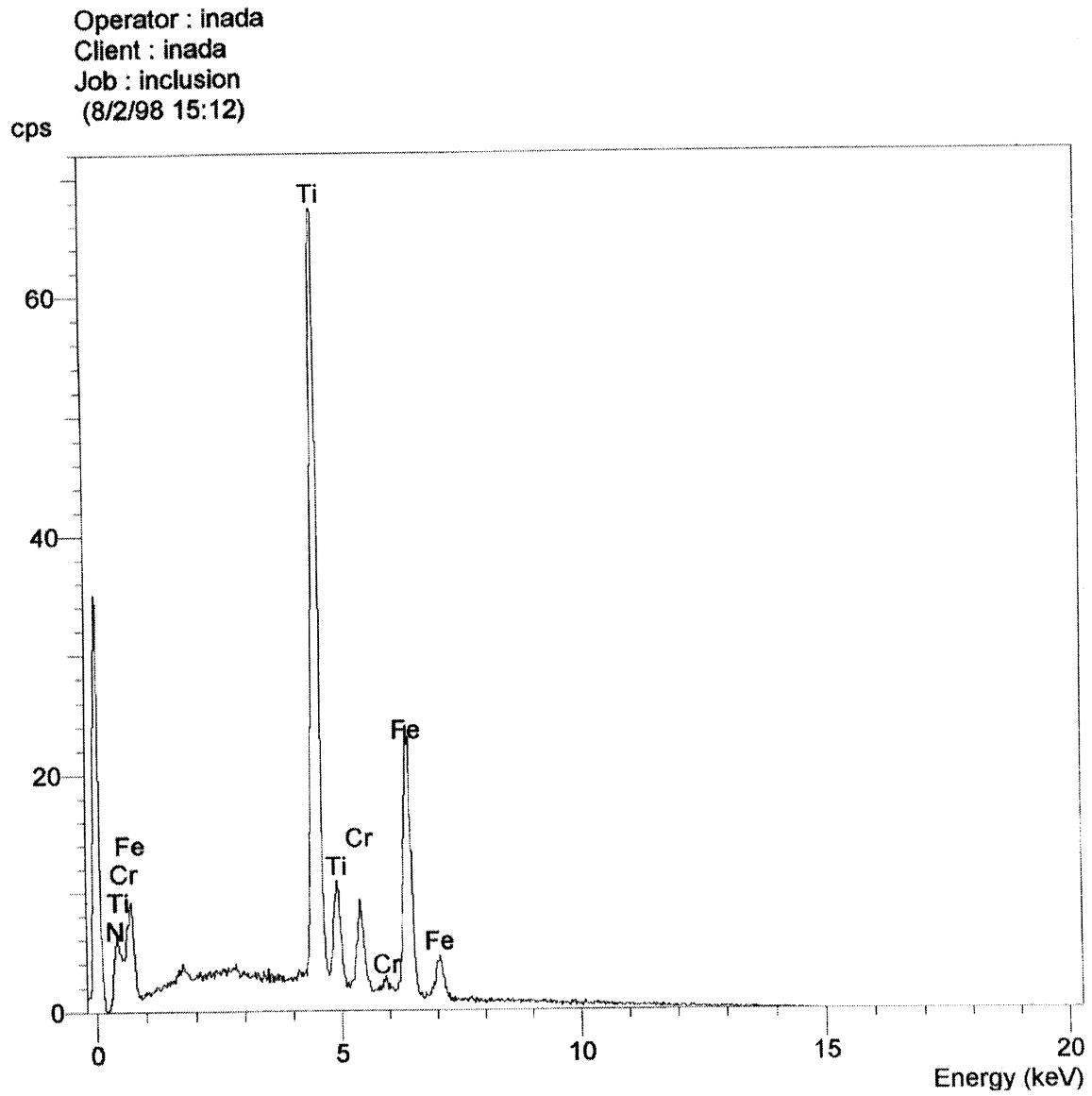


Figure 21 – Spectrum in energy dispersive X-ray spectroscopy from a cuboidal particle (edge length of 2 μm) in a high-Ti-alloy specimen melted and gas-cooled in 4%N₂-gas

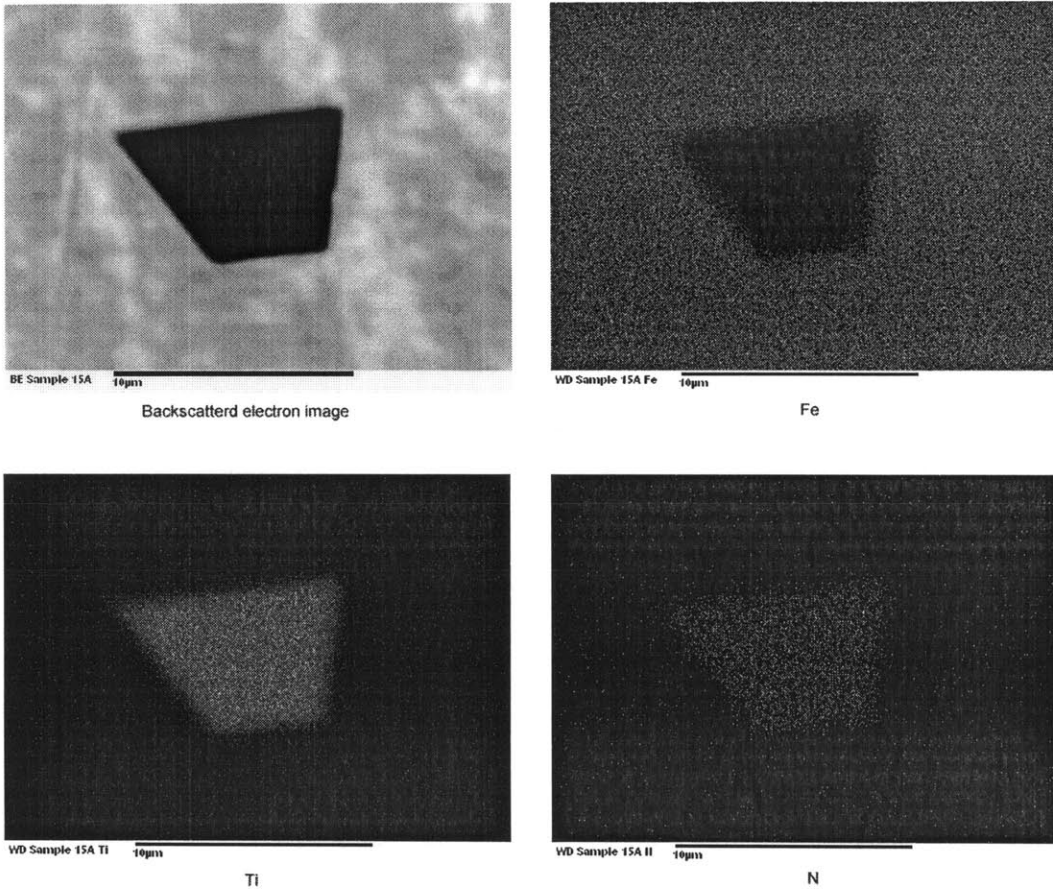


Figure 22 – EPMA images of a large inclusion in a high-Ti-alloy specimen melted and gas-cooled in 4%N₂-gas: backscattered electron image (top-left) and element mapping images of iron, titanium and nitrogen

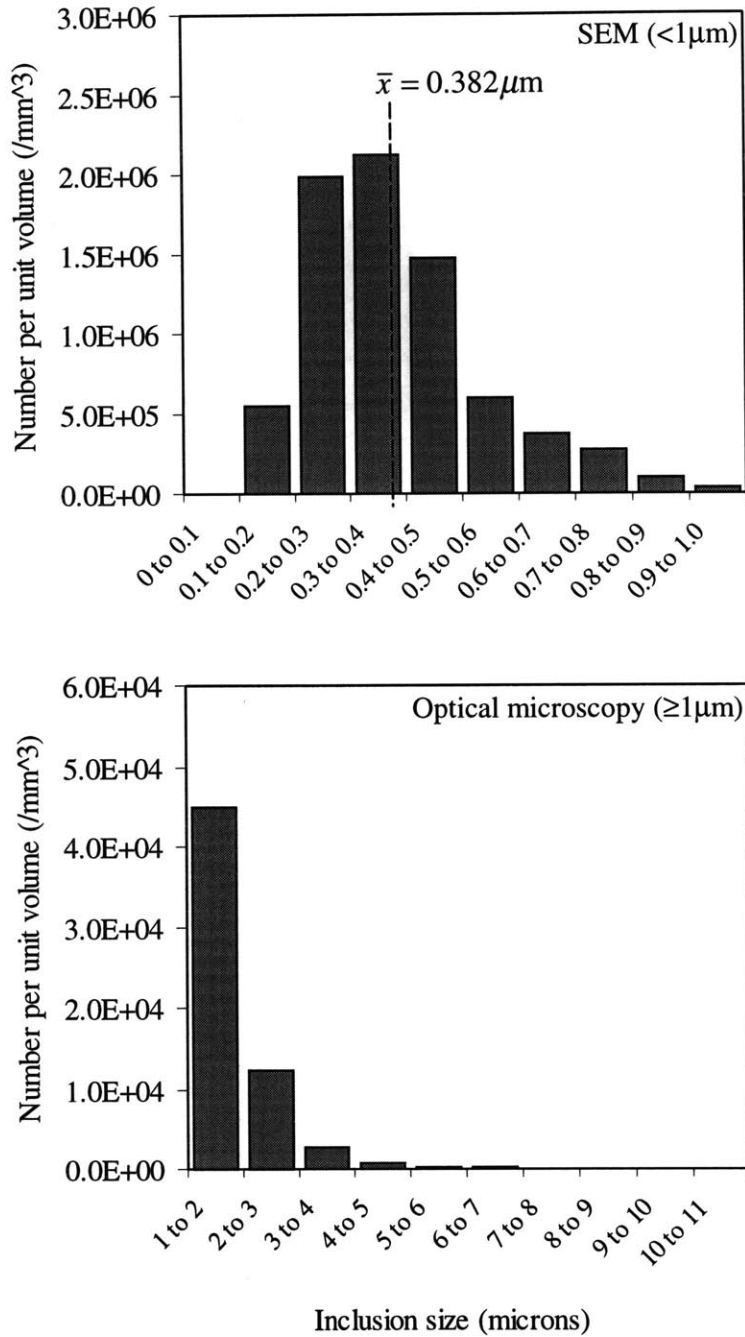


Figure 23 – Inclusion size distribution in a high-Ti-alloy specimen melted and gas-cooled in 4%N₂-gas: small inclusions (< 1 μ m) observed by SEM (top) and large inclusions ($\geq 1\mu\text{m}$) observed by optical microscopy (bottom)

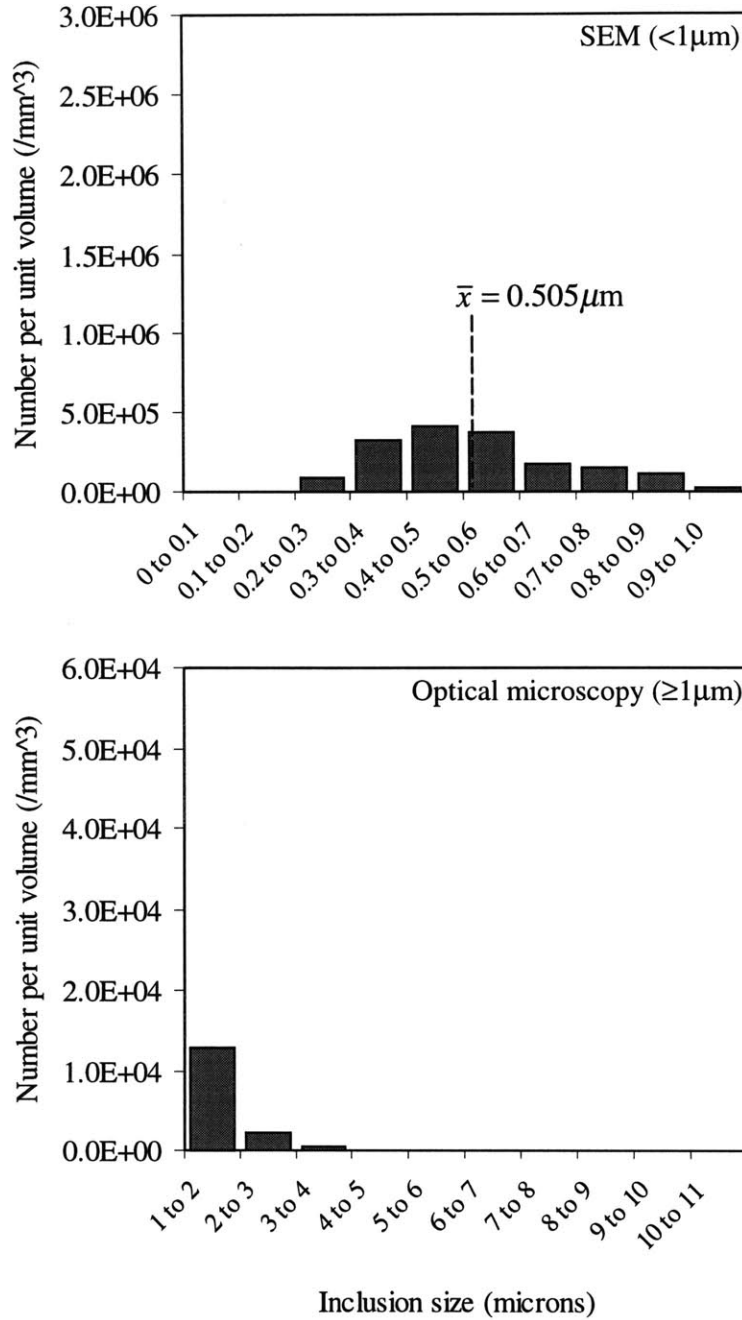


Figure 24 – Inclusion size distribution in a low-Ti-alloy specimen melted and gas-cooled in 4%N₂-gas: small inclusions (< 1 μm) observed by SEM (top) and large inclusions (≥ 1 μm) observed by optical microscopy (bottom)

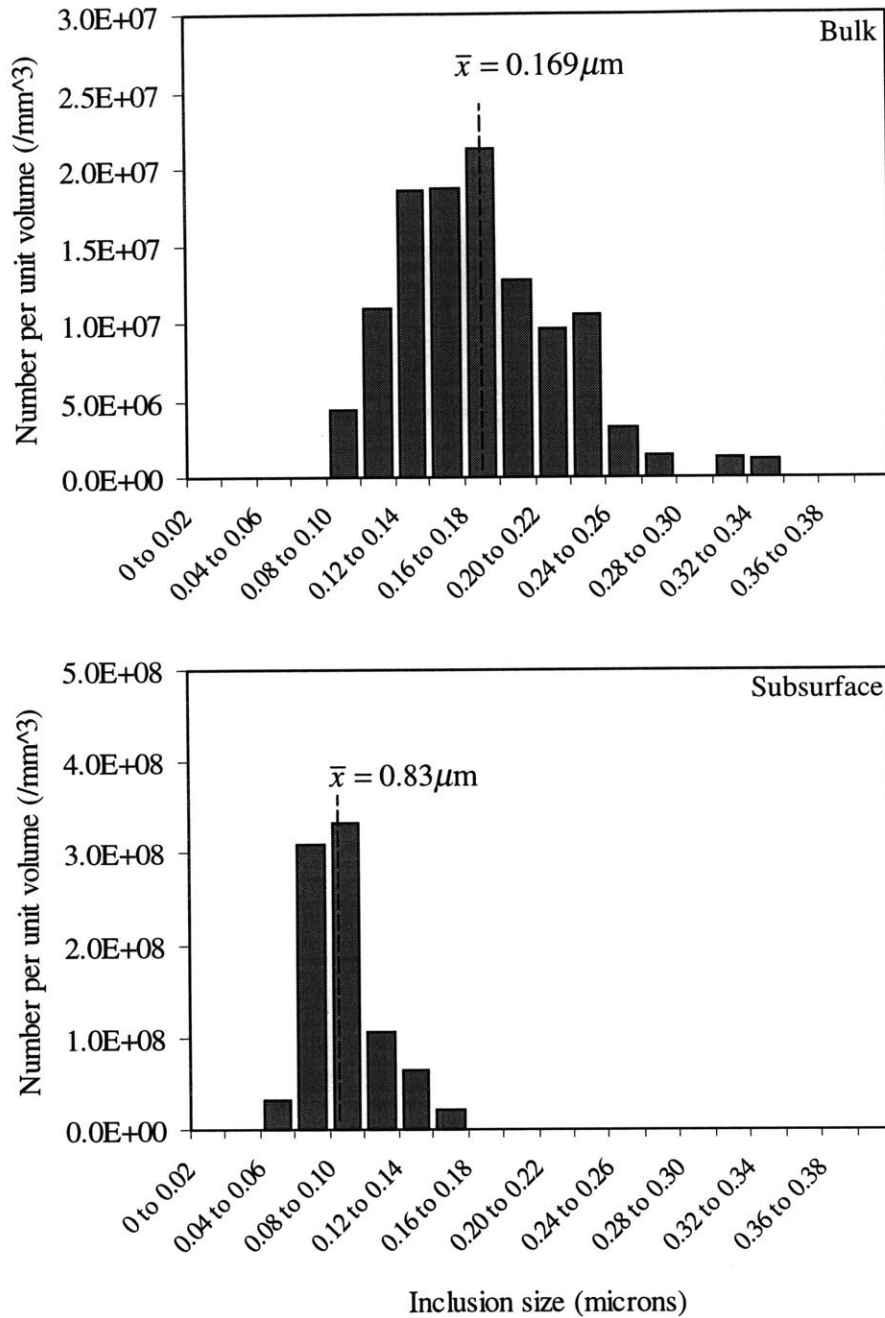


Figure 25 – Inclusion size distribution in a high-Ti-alloy specimen melted and in 4%N₂-gas and quenched in In-Ga bath: in the bulk of specimen 1 to 2 mm from the bottom surface (top), and in a subsurface region 200μm from the bottom surface (bottom)

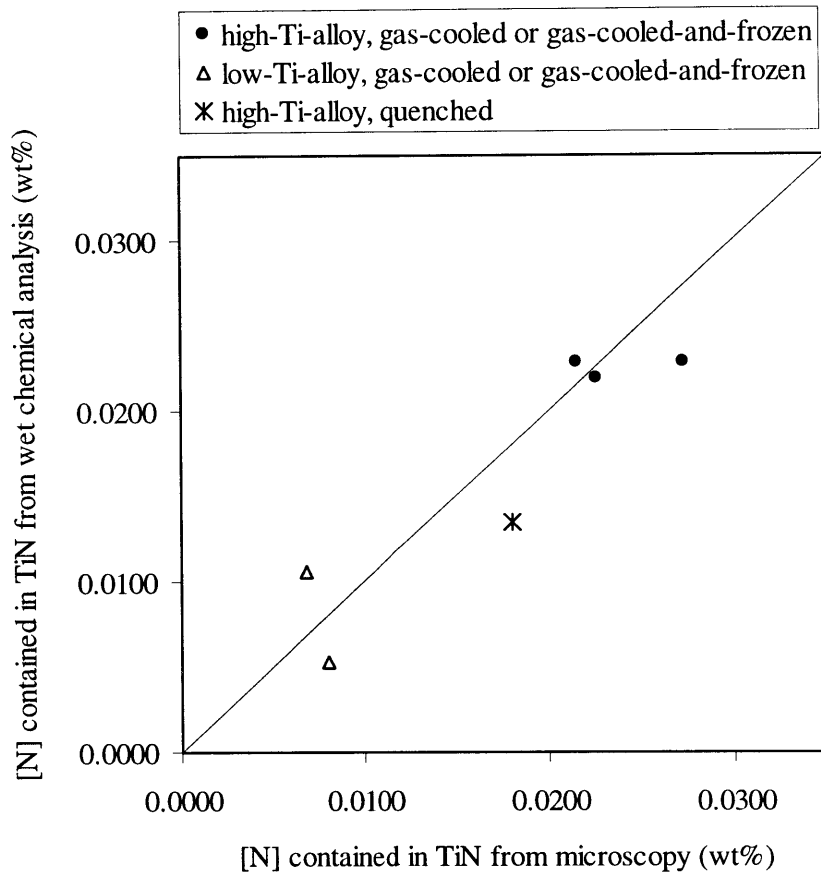


Figure 26 – Comparison of [N] contained in TiN in specimens melted in 4%N₂-gas measured by microscopy and that measured by wet chemical analyses, assuming that all titanium insoluble to sulfuric acid was TiN

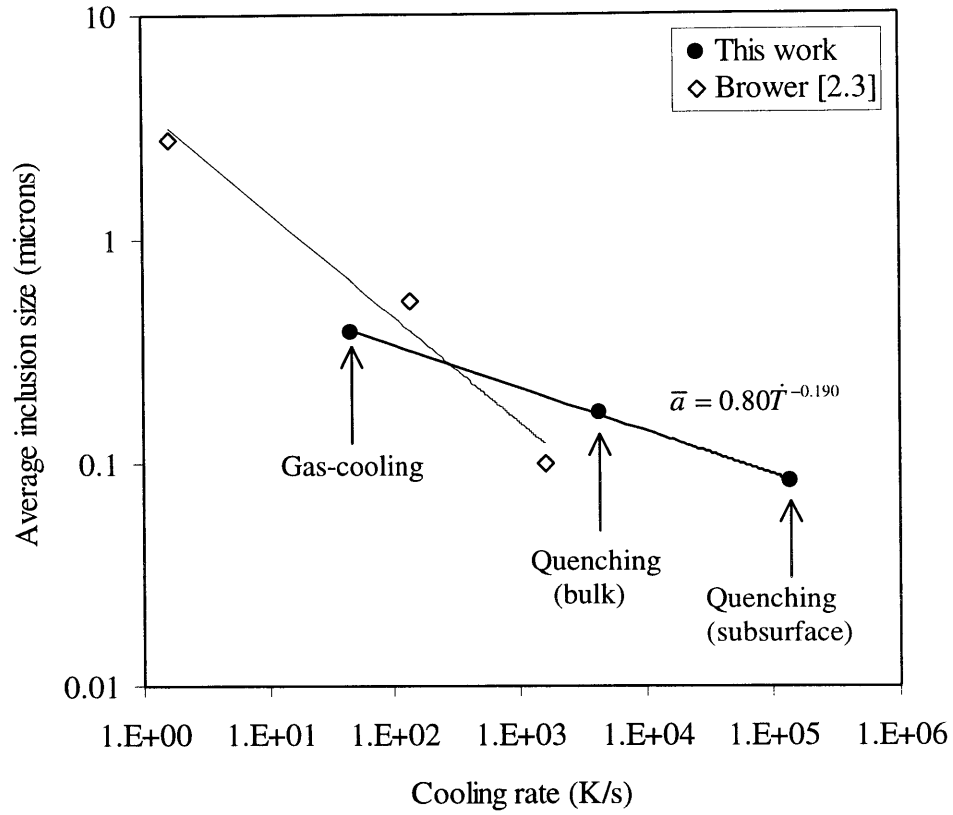


Figure 27 – Variation of average TiN inclusion size with cooling rate in high-Ti-alloy specimens melted in 4%N₂-gas

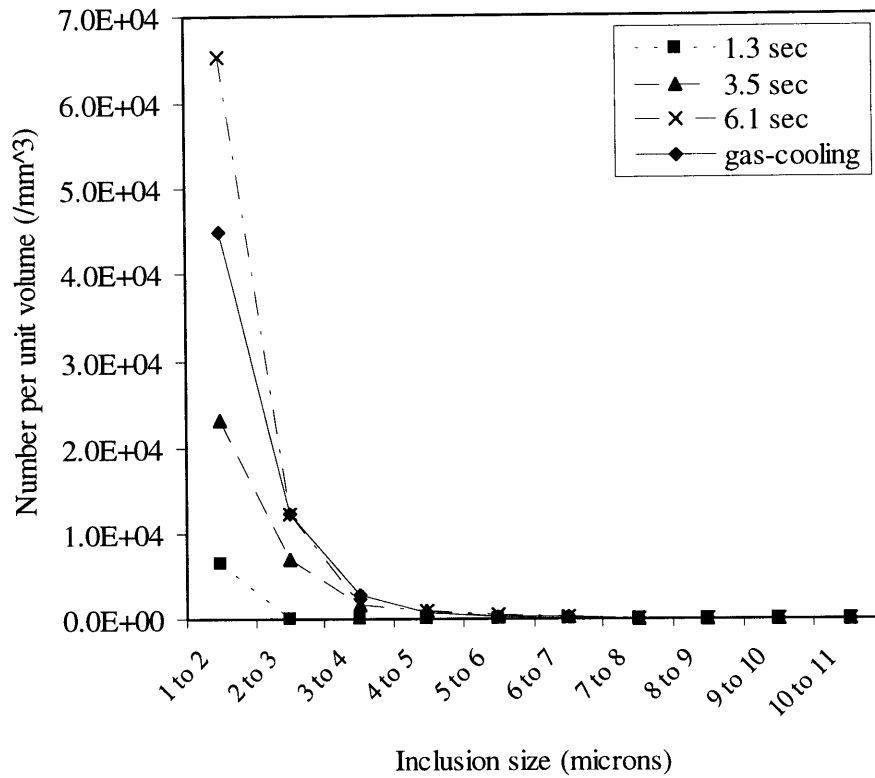


Figure 28 – Variation of inclusion size distribution ($\geq 1 \mu\text{m}$) with holding time at solidifying plateau in the frozen core of high-Ti-alloy specimens melted and gas-cooled in 4%N₂-gas and then quenched in In-Ga bath

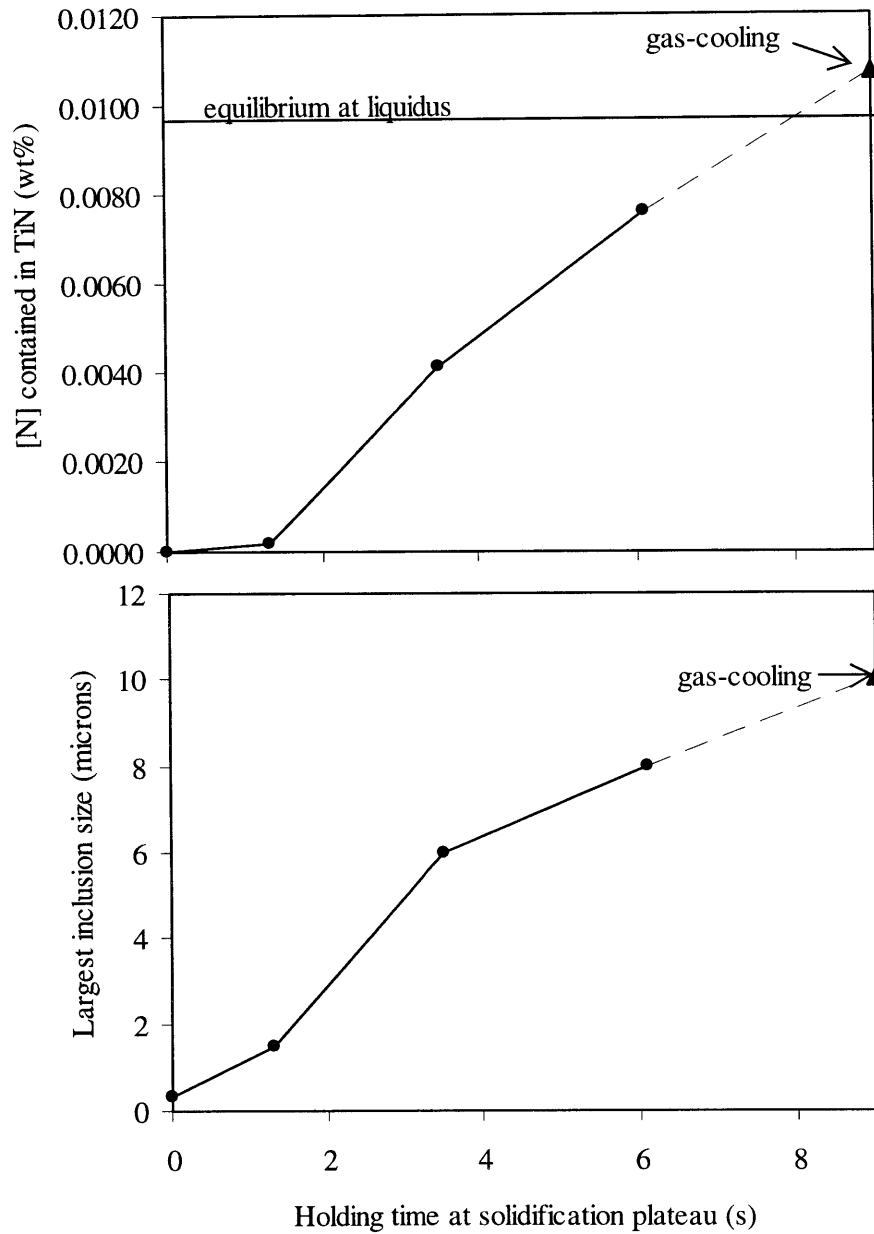


Figure 29 – Increase of primary TiN inclusions ($\geq 1 \mu\text{m}$) as a function of holding time at the solidifying plateau in the frozen core of high-Ti-alloy specimens melted and gas-cooled in 4%N₂-gas and then quenched in In-Ga bath: the amount of TiN inclusions expressed by contained [N] (top), and the largest particle size (bottom)

VI. Discussion

Since inclusions affect the properties of steel products, it is important to control their size and number density and to know their formation kinetics. The process of inclusion formation can be divided into three steps: nucleation, growth and coarsening. It is, therefore, important to find which kinetic step is the slowest and mostly affects the final inclusion size and number density. This chapter presents an evaluation of the rate of each kinetic step for the formation of both primary and secondary inclusions.

1. Nucleation of Inclusions

The rate of homogeneous nucleation of TiN particles in the melt was evaluated using a procedure similar to that of Kunze, et al. [7]. According to the nucleation theory of Volmer and Weber [37], the nucleation rate, I , is

$$I = q_c O_c N_c \quad (15)$$

where q_c is the probability per unit time per area for Ti-N pairs to be captured by the nucleus, O_c is the area of the critical embryo, N_c is the number of embryo of critical size. In this case, q_c is the harmonic mean of the capturing rates of each element, $q_{c,i}$, given by

$$q_{c,i} = X_i \frac{N_A}{V_{Fe}} a_0 \frac{kT}{h} e^{-\Delta G_{D,i}/kT} \quad (16)$$

where X_i is the mole fraction of solute i , N_A is the Avogadro number, V_{Fe} is molar volume of liquid iron, a_0 is the mean atomic distance in liquid iron, kT/h is jumping frequency, k is Boltzmann constant and h is Planck constant. $\Delta G_{D,i}$ is the activation energy for transport and attachment, approximated by the activation energy for diffusion in the melt. The number of critical embryos n_c is given by

$$n_c = X_{Ti} X_N \frac{N_A}{V_{Fe}} e^{-\Delta G_c/kT} \quad (17)$$

where ΔG_c is the free energy change associated with the formation of an embryo of critical size, and is given by

$$\Delta G_c = \frac{16\pi}{3} V_{TiN}^2 \frac{\sigma^3}{\Delta G^2} \quad (18)$$

where V_{TiN} is molar volume of TiN and ΔG is the free energy change associated with the formation of molar TiN in the melt, which is expressed by the supersaturation η , defined in Eq. (2), by

$$\Delta G = -RT \ln \eta \quad (19)$$

Nucleation rates were evaluated by assuming the observable nucleation rate to be larger than $10^9 \text{ m}^{-3} \text{ s}^{-1}$. Thus, the critical supersaturation needed for observable homogeneous nucleation was calculated. Since the interfacial tension between TiN and liquid iron is not known exactly, the calculation was performed using values of 0.7, 0.8 and 0.9 Nm^{-1} . Parameter values used in the calculation were listed in Table 6.

The calculation results are compared in Figure 30 to the calculated supersaturation in the melt that increases due to microsegregation during solidification. From the figure, it is obvious that the homogeneous nucleation can not occur except at the end of solidification of the high-Ti-alloy. This result does not agree with the observation of primary inclusions, since the supersaturation prior to solidification was smaller than the critical. It may be explained by the existence of heterogeneous sites for nucleation. Possible nucleation sites were the surface of specimens and other inclusions that had existed prior to the TiN formation. However, inclusions that contained compounds other than TiN were not detected. The surface might be a heterogeneous nucleation site and the electromagnetic stirring in the melt entrapped the particles inside. This event occurred only prior to solidification, because the surface solidified first and inclusions on the surface could no longer be trapped inside. The captured inclusions were presumably smaller than $1 \mu\text{m}$, since such inclusions were not detected in the high-Ti-alloy specimen melted and gas-cooled in 4%N₂-gas

and then quenched in In-Ga after holding at the solidification plateau for 0.6 s, at the very beginning of solidification. Similarly, secondary inclusions observed in the low-Ti-alloy could not have nucleated homogeneously, since microsegregation was not sufficient to exceed the critical supersaturation needed for homogeneous nucleation. In this case, possible heterogeneous sites were solid-liquid interfaces

2. Diffusion-Controlled Growth of Inclusions

a) Calculation

Diffusion-controlled growth of TiN inclusions was calculated assuming that the particles were spherical and that no kinetic barrier existed at the liquid-particle interface. The mass diffusion equation was

$$\frac{\partial C}{\partial t} = D_L \frac{1}{r^2} \frac{\partial}{\partial r} \left(r^2 \frac{\partial C}{\partial r} \right) \quad (20)$$

where C is solute concentration and D_L is diffusion coefficient in liquid. Mass balance across the interface is expressed by

$$-j = D_L \frac{\partial C}{\partial r} = (C_{inc} - C_R) \frac{\partial R}{\partial t} \quad (21)$$

where C_{inc} and C_R are solute concentrations in the inclusions and at the inclusion surface, respectively, and R is the inclusion radius or position of the interface. The variable r can be eliminated from Eqs. (20) and (21) by using a boundary layer approximation, such that thickness of diffusion boundary layer is equal to the particle radius R . Subsequent equation for R is

$$R \frac{dR}{dt} = D_L \frac{C_L - C_R}{C_{inc}} \quad (22)$$

where C_L is the solute concentration in the bulk liquid. Concentration profile near an inclusion is shown in Figure 31. Solute depletion by the inclusion formation is taken into account in solute mass balance between liquid and inclusions. Mass conservation equation was expressed by

$$\frac{dC_L}{dt} = -C_{inc} \frac{V_{inc}}{dt} \quad (23)$$

where V_{inc} is the volume fraction of inclusions in the melt, which is the product of number density and average volume of inclusions.

In the calculation of the growth of secondary inclusions in the interdendritic or intercellular spaces, the solute content in the bulk liquid, C_L , is simultaneously increased by microsegregation and depleted by the growth of inclusions. Therefore, Eqs. (8) and (22) have to be solved together numerically, since they are coupled by solute mass conservation, which is expressed by Eq. (23). It should be noted that it was assumed that the solute concentration gradient in the vicinity of inclusions does not affect solute distribution at the solid-liquid interface. Values of parameters used in the calculation are listed in Table 6. Time step for primary inclusions was 0.05 s. That for secondary inclusions was 1/100 of the local solidification time, since that calculation had to be synchronized with the calculation of microsegregation.

b) Growth of Primary Inclusions

Results of the calculation of particle diameter during diffusion-controlled growth of primary inclusions in high-Ti-alloy specimens melted and gas-cooled in 4%N₂-gas are shown in Figure 32. The largest inclusion sizes measured in gas-cooled-and-frozen specimens of Figure 29 are also reported versus holding time at the solidification plateau. Line (1) was calculated assuming no solute depletion due to TiN formation. In other words, the number density of particles was assumed to be close to zero in this case. Line (2) was calculated assuming that the particle number density of $1.64 \times 10^4 \text{ mm}^{-3}$, which was equal to that of the larger inclusions ($> 1 \text{ }\mu\text{m}$) observed in the gas-cooled specimen of Figure 9. The measured real sizes are in-between the two calculated lines. Hence, the increase of primary inclusion size may be attributed to a diffusion-controlled growth. The observed sizes are smaller than line (1) because solutes were depleted to some extent by the inclusion formation, and they

are larger than line (2) because the number density of particles also increased with time, so that actual solute depletion was not as rapid as that calculated using the number density of inclusions in the final stage.

c) Growth of Secondary Inclusions

Particle diameter during growth of secondary inclusions was calculated by combining microsegregation and diffusion-controlled growth of particles in three cases: gas-cooling of high-Ti-alloy, gas-cooling of low-Ti-alloy, and quenching of high-Ti-alloy. Number density of particles was assumed to be equal to the measured total volume fraction of inclusions divided by the average particle volume, which means that all particles were assumed, hypothetically to have the same size. Those values of number density were 1.10×10^7 , 2.70×10^6 and $2.15 \times 10^8 \text{ mm}^{-3}$ for the gas-cooled specimen of high-Ti-alloy (Figure 9), the gas-cooled specimen of low-Ti-alloy (Figure 10), and the quenched specimen of high-Ti-alloy (Figure 15), respectively.

The calculation results for the gas-cooled specimens of both the high-Ti-alloy and low-Ti-alloy are shown in Figure 33. In the case of high-Ti-alloy, particle diameter rapidly increases to around $0.5 \mu\text{m}$ and then suddenly the growth rate decreases and growth continues very slowly until the end of solidification. The rapid growth at the beginning is due to the supersaturation that existed prior to solidification. At the onset of solidification, inclusions begin to grow and solutes are rapidly consumed; hence, the supersaturation disappears, resulting in inclusion growth arrest. The only remaining source of solute for inclusions to grow further is solute accumulation due to microsegregation. In the case of low-Ti-alloy, solute supersaturation may only be attributed to microsegregation; hence, the growth of inclusions also begins during solidification. The growth is not as fast as the growth in the high-Ti-alloy. It ceases gradually by the end of solidification due to solute depletion. The calculation results for the quenched specimen of high-Ti-alloy are shown in Figure 34. The results are similar to those of the gas-cooled specimen of

high-Ti-alloy, although time scale is much smaller, as is the final inclusion size which is about 0.2 μm , since the number density of particles were assumed to be much higher than that in the gas-cooled specimen.

The number density of inclusions directly affects the final inclusion size in all cases, since growth of inclusions is rapid enough to consume all solute supersaturation. Especially for the high-Ti-ally, the number density predominantly controls the final inclusion size, since most of the growth takes place at the very beginning of solidification at the expense of supersaturation prior to the inclusion formation. Hence, diffusion-controlled growth is very rapid and does not affect the size of secondary inclusions. Nucleation events before and during solidification and subsequent coarsening may be slower and have more influence on the kinetics of secondary inclusion formation.

3. Coarsening of Inclusions

a) Coarsening of Primary Inclusions

Small particles have an excess free energy due to their high surface-to-volume ratio. Equilibrium of a spherical inclusion particle is expressed by Gibbs-Thompson's equation:

$$RT \ln \left(\prod_i \frac{a_{r,i}}{a_{\infty,i}} \right) = V_m \frac{2\gamma}{r} \quad (24)$$

where $a_{r,i}$ is the activity of solute i in equilibrium with a particle of radius r , and $a_{\infty,i}$ is that in equilibrium in contact with a planar compound ($r=\infty$), V_m is molar volume of the inclusion and γ is the interfacial tension. Assuming the activity to be linear with solute concentration, Eq. (24) leads to that for concentration products expressed by:

$$\prod_i C_{r,i} = \left(\prod_i C_{\infty,i} \right) \cdot e^{\frac{2\gamma V_m}{rRT}} \quad (25)$$

where $C_{r,i}$ and $C_{\infty,i}$ are the concentrations of solute i in equilibrium with the particle of radius r and the planar compound. This equation means that smaller inclusions have higher solubility, which may lead to the dissolution.

Variation of the concentration product $C_r(\text{Ti})C_r(\text{N})$ in equilibrium with TiN particles with particle diameter is expressed by the ratio of this product over that in equilibrium with planar TiN, in Figure 35. This ratio is equal to the solubility of TiN particles when the solute contents are in equilibrium with planar TiN. The value becomes almost independent of particle size at particle diameters greater than 0.1 μm . This means that the coarsening of primary TiN particles takes place almost exclusively at the expense of particles smaller than 0.1 μm in diameter. No evidence of this coarsening was available in the observation, since such fine inclusions were not observed in the specimens. However the possibility can not be eliminated at all because such fine inclusions may coarsen and become observable during solidification

b) Ostwald Ripening of Secondary Inclusions

Since the diffusion-controlled growth of secondary inclusions is very rapid to reach equilibrium, there is sufficient time for coarsening to take place. Under equilibrium conditions, coarsening can be simplified to Ostwald ripening, in which time dependence of the average particle radius \bar{r} is approximated by Wagner's equation [40]:

$$\bar{r}^3 - \bar{r}_0^3 = \frac{8}{9} \frac{\gamma D_L C_L V_m^2}{RT} t \quad (26)$$

where \bar{r}_0 is the initial particle radius, γ is the interfacial tension between inclusion and liquid iron, D_L is the diffusion coefficient in the melt, C_L is the solute concentration in the melt, and V_m is the molar volume of TiN.

The calculated increase of average particle diameter with time is shown by the plain line in Figure 36. The average inclusion sizes observed in the gas-cooled and quenched specimen of high-Ti-alloy are also reported versus their local solidification

time as experimental points in the same figure. The order of measured average inclusion size is in good agreement with the calculated line. This means that the increase of secondary inclusion size may be attributed to Ostwald ripening. However, measured inclusion average size increases as the local solidification time raises to 0.190 power. The exponent is less than the one third predicted in Ostwald ripening. The reason of this difference is not clear and needs further study.

4. Summary

The kinetics of inclusion formation may be summarized as follows:

- 1) Nucleation of both primary and secondary inclusions is heterogeneous, because the solute supersaturation is not large enough to exceed the supersaturation needed for homogeneous nucleation.
- 2) Growth of primary inclusions is presumably controlled by diffusion, although it may also be affected by nucleation events and coarsening simultaneously. Growth rate of secondary inclusions is too high and can not dominate the kinetics of their formation.
- 3) Coarsening of primary inclusions may occur at the expense of very fine particles ($<0.1 \mu\text{m}$). The increase of secondary inclusion size with the local solidification time may be explained by Ostwald ripening, although time dependence measured is smaller than predicted in Ostwald ripening.

Table 6 – Values of the parameters used in the calculation of inclusion formation

parameter		value	ref.
$\rho(\text{Ti})$	Density of TiN	5240 kg m ⁻³	
$\rho(\text{Fe})$	Density of liquid iron	7000 kg m ⁻³	
$M(\text{Ti})$	Mass number of Ti	47.9	
$M(\text{N})$	Mass number of N	14	
$C_{inc}(\text{Ti})$	Concentration of Ti in TiN	4055 kg m ⁻³	
$C_{inc}(\text{N})$	Concentration of N in TiN	1185 kg m ⁻³	
V_m	Molar volume of TiN	1.18×10 ⁻⁵ m ³ mol ⁻¹	
$D_L(\text{Ti})$	Diffusion coefficient of Ti in liquid iron (at 1788 K)	8.33×10 ⁻³ e ^{-212000/RT} m ² s ⁻¹ (5.40×10 ⁻⁹ m ² s ⁻¹)	[38]
$D_L(\text{N})$	Diffusion coefficient of N in liquid iron	1.1×10 ⁻⁸ m ² s ⁻¹	[39]
$\Delta G_D(\text{Ti})$	Activation energy for diffusion of Ti	7.99×10 ⁻²⁰ J	
$\Delta G_D(\text{N})$	Activation energy for diffusion of N	7.99×10 ⁻²⁰ J	*
γ	Interfacial tension between TiN and liquid iron	0.7, 0.8, 0.9 N m ⁻¹	
T	Temperature	1788 K	
L_{TiN}	Solubility Product [Ti][N] (at 1788 K)	e ^{-41740/T+17.39} wt% ² (2.59×10 ⁻³ wt% ²)	

*: use the same value as $\Delta G_D(\text{Ti})$, since no value was found in literatures

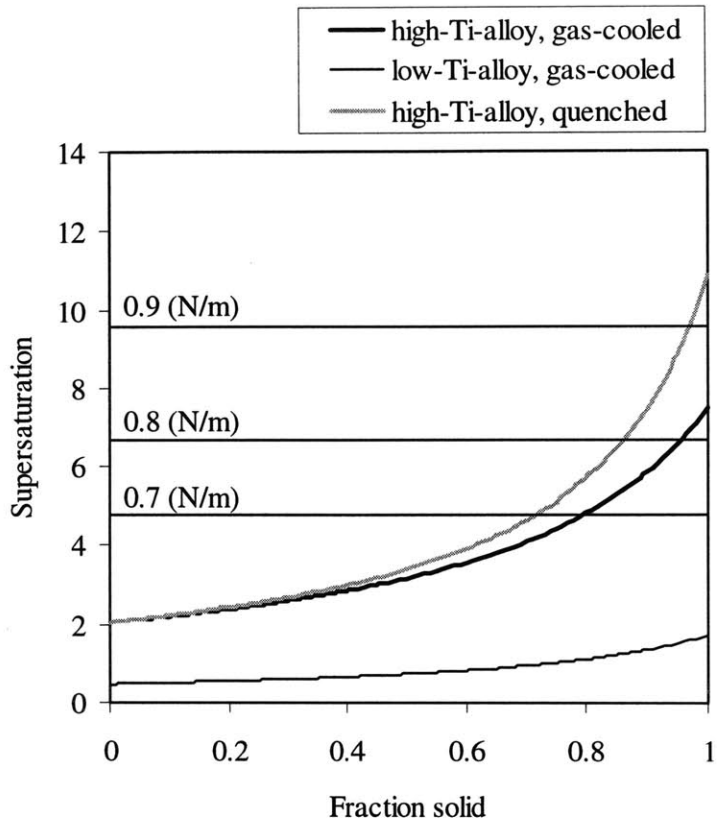


Figure 30 – Increase of the supersaturation factor η due to the microsegregation along with the critical supersaturation needed for homogeneous nucleation of TiN particles in the melt

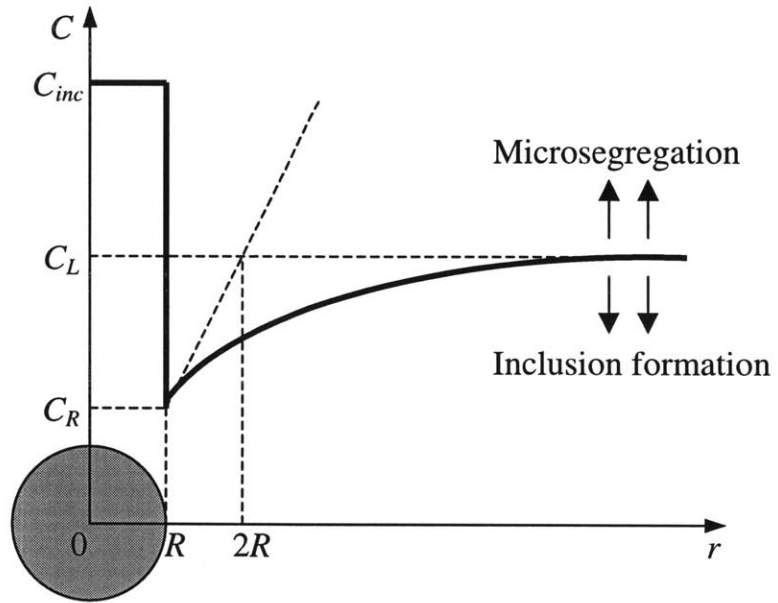


Figure 31 – Concentration profile near a growing particle

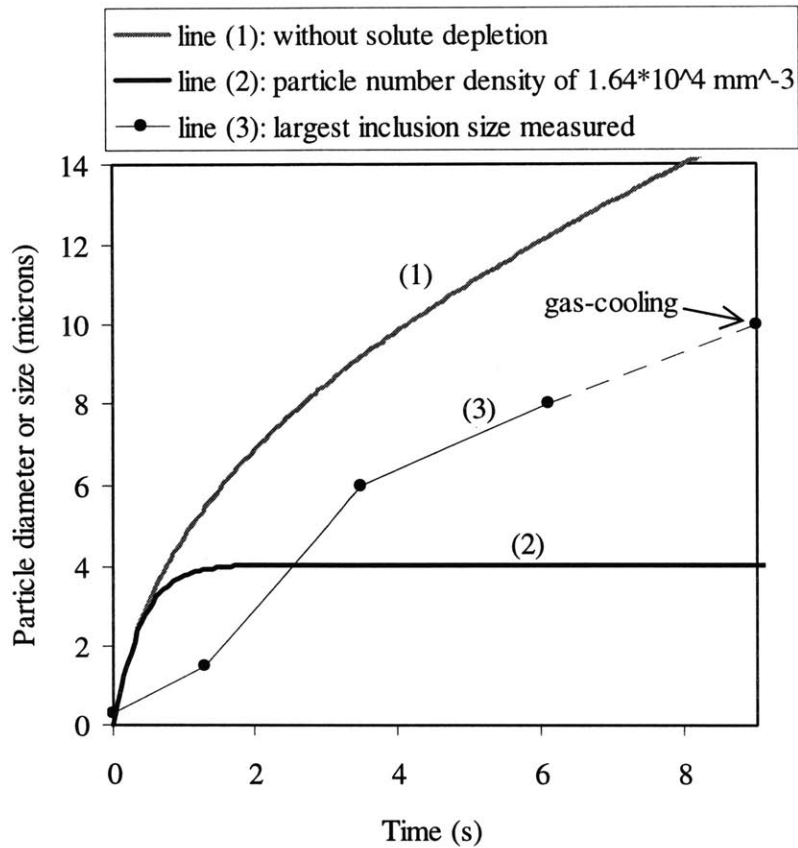


Figure 32- Calculated particle diameter during diffusion-controlled growth of primary TiN inclusions in the melt for high-Ti-alloy: without solute depletion by the TiN formation [line (1)], assuming constant number density of particles of $1.14 \times 10^4 \text{ mm}^{-3}$ [line (2)], and measured largest inclusion size in gas-cooled-and-quenched specimens vs. holding time at the solidification plateau [line (3)]

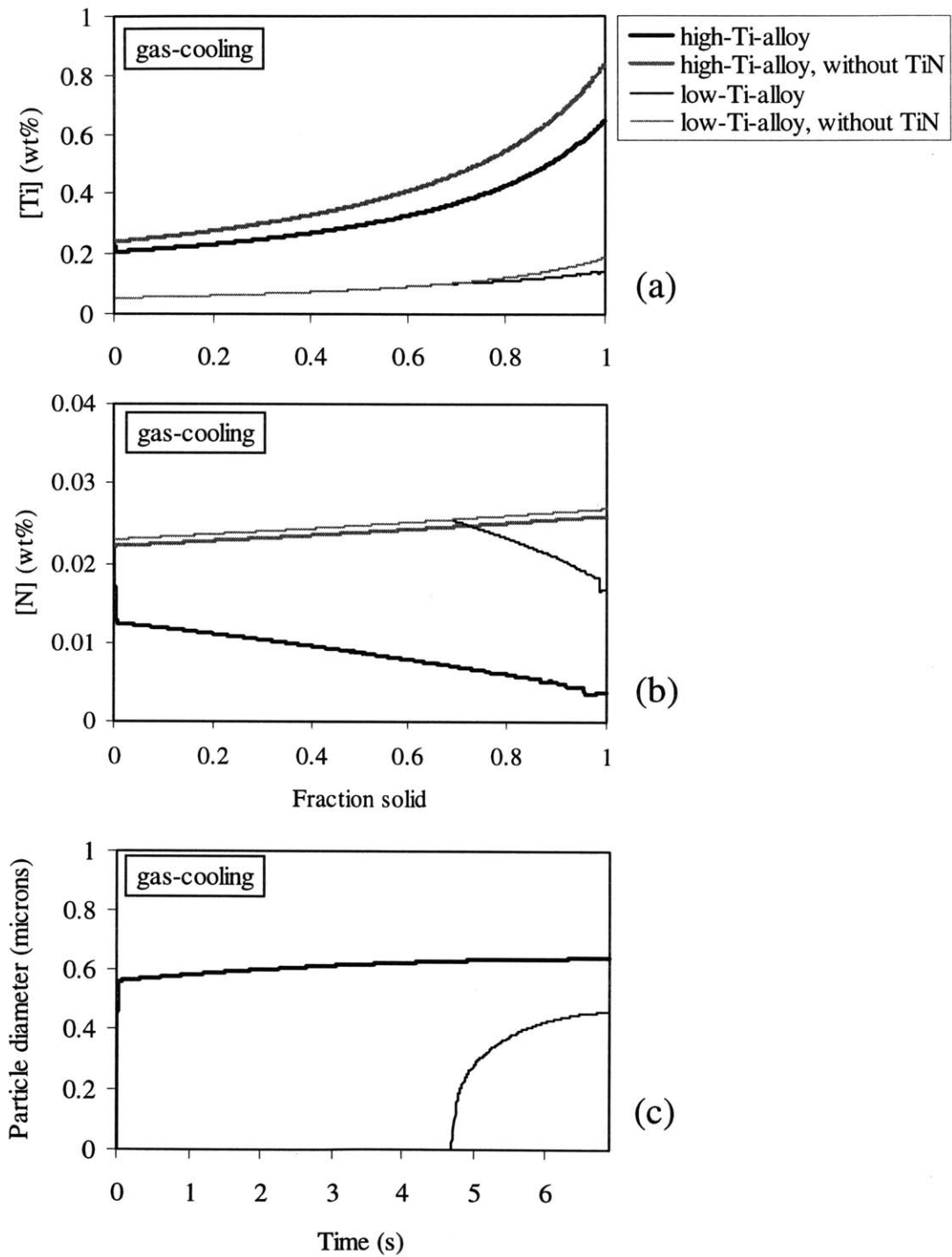


Figure 33- Calculation results of growth related parameters of secondary TiN inclusions in gas-cooled specimens: variation of [Ti] (a) and [N] (b), as a function of fraction solid, and increase of particle size with time (c)

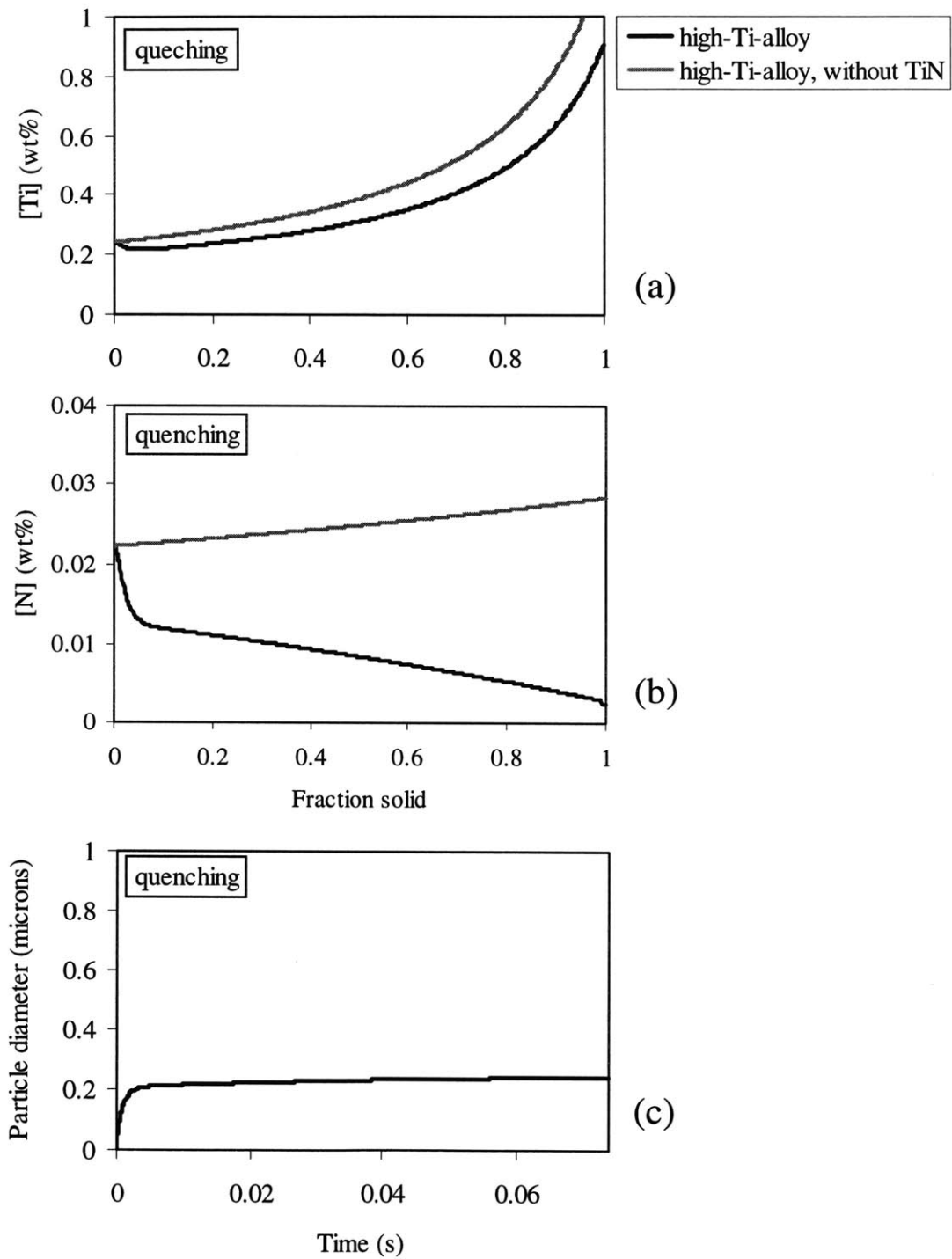


Figure 34- Calculation results of growth related parameters of secondary TiN inclusions in the quenched specimen of high-Ti-alloy: variation of $[Ti]$ (a) and $[N]$ (b) as a function of fraction solid, and increase of particle size with time (c)

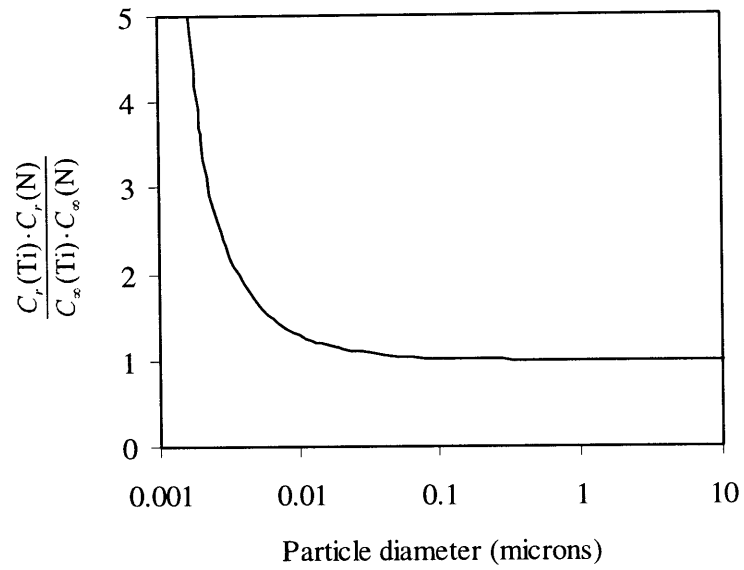


Figure 35- Variation of solubility of spherical TiN particles vs. diameter, expressed by the ratio of the concentration product for particle divided by that corresponding to planar TiN, assuming interfacial tension of 0.8 Nm^{-1}

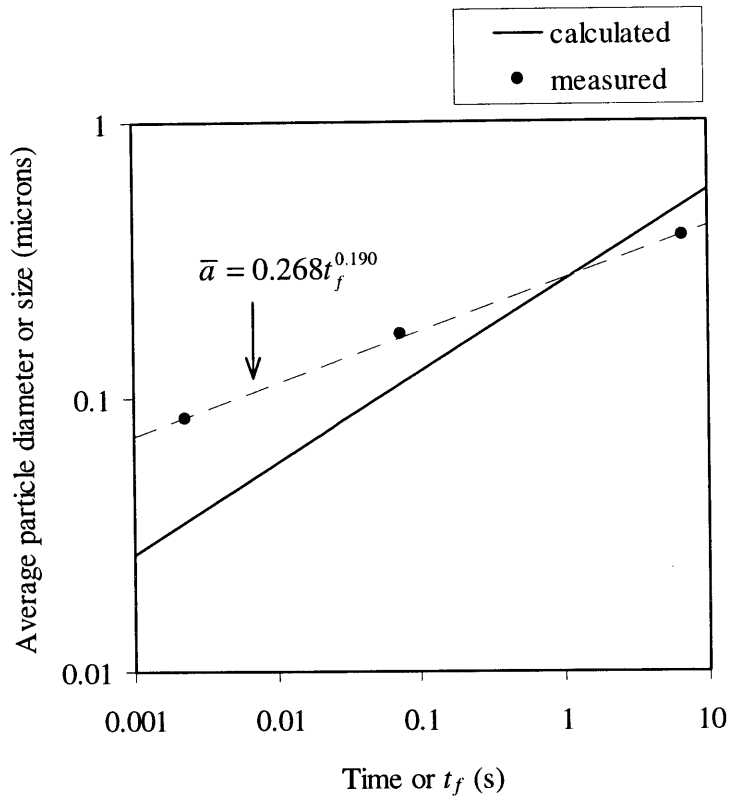


Figure 36- Ostwald ripening of secondary TiN inclusions: calculated curve of average particle diameter vs. time, assuming the initial average diameter of $0.01 \mu\text{m}$ and the interfacial tension of 0.8 Nm^{-1} , and experimental points representing average inclusion size observed in gas-cooled and quenched specimen reported vs. local solidification time t_f

VII. Conclusions

The formation of titanium nitride (TiN) nonmetallic inclusions during the solidification of stainless steel 409 was investigated for different concentrations of titanium and nitrogen at different cooling rates. Specimens were melted using an electromagnetic levitation facility. Rapid solidification was subsequently obtained by the gas-cooling (40 Ks^{-1}) or by quenching into In-Ga (5×10^3 to $1 \times 10^6 \text{ Ks}^{-1}$). The conclusions obtained in the present study are as follows:

- 1) When the supersaturation of TiN occurred above the liquidus temperature, formation of equiaxed dendrite grains and early coverage of the whole surface by columnar grains were observed in the gas-cooled specimens. These effects on microstructure are presumably due to the primary TiN inclusions that act as ferrite nucleants during solidification. Grain boundary pinning by the fine inclusions was also observed.
- 2) No effect of TiN on microstructure was observed in the quenched specimens, presumably because cooling of the specimens was so rapid that no time was available for the formation of primary TiN inclusions, which would act as ferrite nucleants. Grain boundaries also hardly migrated, even in the absence of TiN.
- 3) Most of TiN inclusions were located along the interdendritic or intercellular spaces and had a typical cuboidal shape. However, irregularly shaped inclusions were also observed. The average inclusion size was predominantly controlled by the secondary inclusions and varied proportionally to $\dot{T}^{-0.190}$. Inclusions larger than $1 \mu\text{m}$, observed in the quenched core of the gas-cooled-and-frozen specimens, were primary inclusions. These inclusions grew both in size and number density with increasing holding times at the solidification plateau.
- 4) Primary inclusions presumably nucleate heterogeneously. Their growth is presumably controlled by diffusion. Nucleation of secondary inclusions is also mostly heterogeneous. The decrease of their size with increasing cooling rate may be explained by coarsening.

Appendix A

Variation of [N] and [O] during Levitation Melting

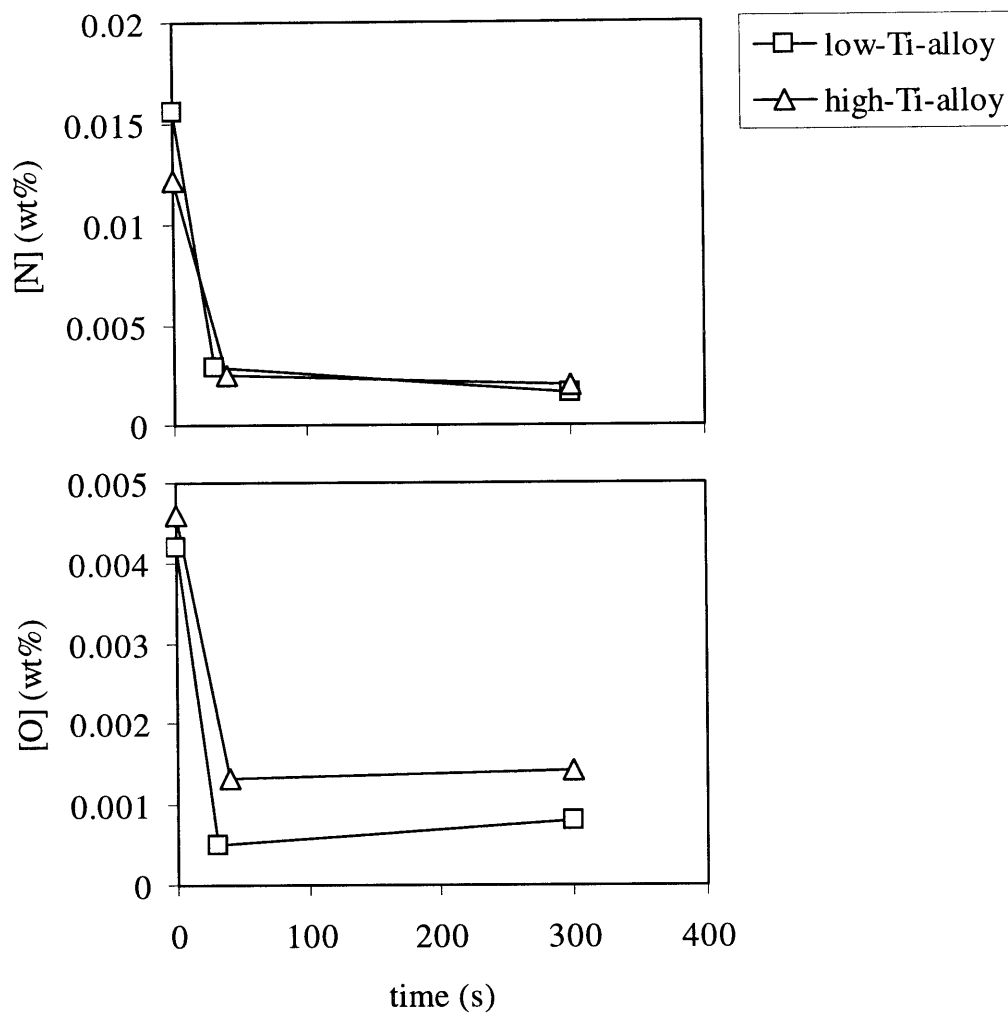


Figure A - Variation of nitrogen (top) and oxygen (bottom) concentration in gas-cooled specimens melted in no-N₂-gas with holding time in the molten state (holding temperature was about 100 K above the liquidus)

Appendix B

1. Calculation of Thermal Diffusion with Finite Difference Approximation

The thermal diffusion equation in the spherical coordinate system is given by

$$\frac{\partial T}{\partial t} = \alpha \frac{1}{r^2} \frac{\partial}{\partial r} \left(r^2 \frac{\partial T}{\partial r} \right) \quad (\text{B.1})$$

where T is temperature and α is thermal diffusivity defined as

$$\alpha \equiv \frac{K}{C_p} \quad (\text{B.2})$$

where K is thermal conductivity and C_p is specific heat per unit volume.

To determine the temperature as a function of location and time, the domain of a specimen ($0 \leq r \leq R$) is subdivided into small shells of thickness Δr , as shown in

Figure B. Subscript nodes q are numbered consecutively 1 to N from the center to the surface, while superscript nodes show time.

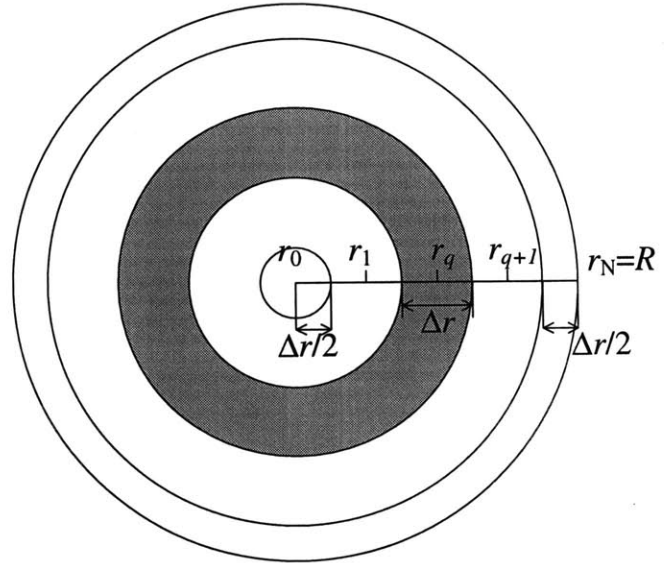


Figure B – The spherical specimen ($0 \leq r \leq R$) subdivided into ring segments

For nodes in the middle ($2 \leq q \leq N-1$), Eq. (B.1) becomes

$$4\pi r_q^2 \Delta r C_p \frac{T_q^{i+\Delta t} - T_q^i}{\Delta t} = K \left[4\pi \left(r_q + \frac{\Delta r}{2} \right)^2 \frac{T_{q+1}^i - T_q^i}{\Delta r} + 4\pi \left(r_q - \frac{\Delta r}{2} \right)^2 \frac{T_{q-1}^i - T_q^i}{\Delta r} \right] \quad (\text{B.3})$$

Solving Eq. (B.3) for $T_q^{i+\Delta t}$ yields

$$T_q^{i+\Delta t} = Fo \left[\left(1 + \frac{\Delta r}{r_q} \right) T_{q+1}^i + \left(1 - \frac{\Delta r}{r_q} \right) T_{q-1}^i \right] + (1 - 2Fo) T_q^i \quad (\text{B.4})$$

where Fo is the Fourier number defined as

$$Fo \equiv \frac{\alpha \cdot \Delta t}{\Delta r^2} \quad (\text{B.5})$$

To prevent unstable numerical oscillations in the solution, the required stability criterion is

$$1 - 2Fo \geq 0 \quad (\text{B.6})$$

Since no heat is conducted to the inside of the center circle ($0 \leq r \leq \Delta r/2$), the finite difference equation is derived in a different manner for $q=0$ as

$$\frac{4}{3}\pi \left(\frac{r}{2}\right)^3 C_p \frac{T_0^{t+\Delta t} - T_0^t}{\Delta t} = K 4\pi \left(\frac{r}{2}\right)^2 \frac{T_1^t - T_0^t}{\Delta r} \quad (\text{B.7})$$

Solving Eq. (B.7) for $T_0^{t+\Delta t}$,

$$T_0^{t+\Delta t} = 6FoT_1^t + (1 - 6Fo)T_0^t \quad (\text{B.8})$$

The stability criterion is

$$1 - 6Fo \geq 0 \quad (\text{B.9})$$

At the surface ring ($R - \Delta r/2 \leq r \leq R$), adding the heat transfer term to outside, the finite difference equation for $q=N$ becomes

$$4\pi R^2 \frac{\Delta r}{2} C_p \frac{T_N^{t+\Delta t} - T_N^t}{\Delta t} = K \left[4\pi \left(R - \frac{\Delta r}{2}\right)^2 \frac{T_{N-1}^t - T_N^t}{\Delta r} \right] + 4\pi R^2 h (T_\infty - T_N^t) \quad (\text{B.10})$$

Solving Eq. (B.10) for $T_N^{t+\Delta t}$ yields

$$T_N^{t+\Delta t} = 2FoBiT_\infty + 2Fo \left(1 - \frac{\Delta r}{R}\right) T_{N-1}^t + \left[1 - 2Fo \left(1 - \frac{\Delta r}{R} + Bi\right) \right] T_N^t \quad (\text{B.11})$$

where Bi is the Bio number defined as

$$Bi \equiv \frac{h\Delta r}{K} \quad (\text{B.12})$$

The stability criterion is

$$1 - 2Fo \left(1 - \frac{\Delta r}{R} + Bi\right) \geq 0 \quad (\text{B.13})$$

By using the initial condition that the temperature within the whole specimen is T_0 , and by selecting certain values of Δr and Δt , the temperature at time T can be calculated. With small Δr the results are closer to the exact solution; however, Δt has to be correspondingly reduced in order to meet the criteria (B.6),(B.9),(B.13).

2. Temperature Recovering during Solidification

When a segment of the specimen is cooled below the liquidus temperature, it begins to solidify and generate the heat of fusion, which is given by

$$\dot{Q}_q^t = (F_{s_q}^{t+\Delta t} - F_{s_q}^t)\Delta H_f \quad (\text{B.14})$$

where \dot{Q}_q^t is the heat of fusion generated per unit volume during the time interval t to $t+\Delta t$, $F_{s_q}^t$ is the fraction solid, and ΔH_f is the heat of fusion per unit volume.

The steps for calculating the temperature recovering were the following:

- 1) Calculate hypothetical $T_q^{t+\Delta t}$ from the present temperature profile using the finite difference approximation without taking into account heat generation.
- 2) If $T_q^{t+\Delta t}$ is below the liquidus temperature, an increase of fraction solid can be calculated as

$$F_{s_q}^{t+\Delta t} - F_{s_q}^t = -\frac{C_p}{\Delta H_f}(T_q^{t+\Delta t} - T_q^t) \quad (\text{B.15})$$

- 3) The present temperature is calculated from the fraction solid using the lever rule as

$$T_q^t = T_L - (T_L - T_S)F_{s_q}^t \quad (\text{B.16})$$

- 4) The generated heat is treated as a heat source in calculating the temperature profile for the next time step. For instance, Eq. (B.3) can be modified to

$$4\pi r_q^2 \Delta r C_p \frac{T_q^{t+\Delta t} - T_q^t}{\Delta t} = K \left[4\pi \left(r_q + \frac{\Delta r}{2} \right)^2 \frac{T_{q+1}^t - T_q^t}{\Delta r} + 4\pi \left(r_q - \frac{\Delta r}{2} \right)^2 \frac{T_{q-1}^t - T_q^t}{\Delta r} \right] + \dot{Q}_q^t \quad (\text{B.17})$$

Appendix C

Critical Inclusion Size for Rejection/Engulfment by the Solidification Front

Shibata, et al. [35], measured the critical velocities of engulfing Al_2O_3 -particles on the surface of iron melts, and obtained a criterion for capturing, which is given by

$$U \geq 30/d \quad (\text{C.1})$$

where U is the growth rate or velocity of the advancing solidification front in $\mu\text{m s}^{-1}$ and d is the particle diameter in μm . Since both the thermal conductivity of TiN and its interfacial tension with liquid iron are close to the correspondent values for Al_2O_3 , the criterion for TiN may be similar to that determined for Al_2O_3 . In figure C, this criterion is compared to the measured TiN inclusion size and the solidification velocities obtained in the present work. From that figure, it is apparent that all inclusions may be pushed by the solidification front towards the interdendritic or intercellular spaces, resulting in the accumulation of inclusions in those locations.

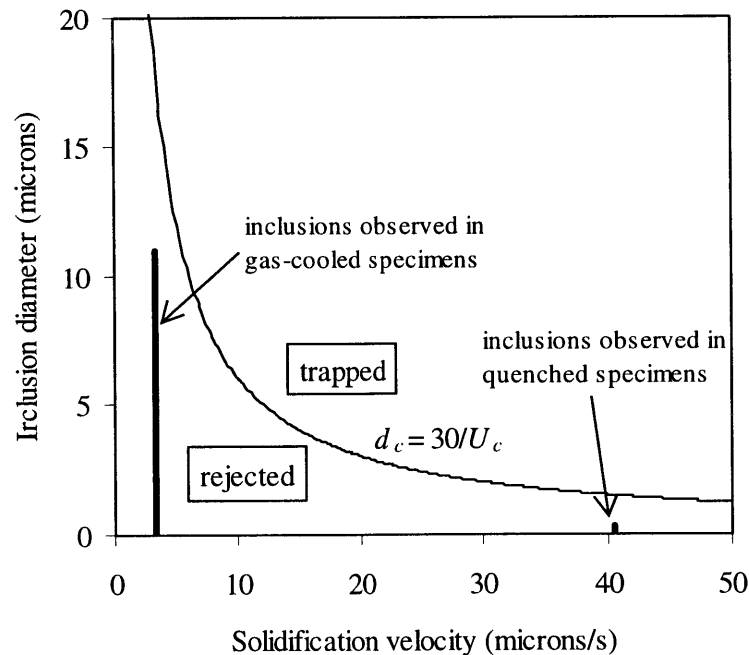


Figure C – Variation of critical inclusion diameter for rejection/engulfment versus the velocity of advancing solidification front [35] and the measured inclusion size

Bibliography

- [1] M.C. Flemings: *Solidification Processing*, 1974, McGraw-Hill, New York, NY, p. 193
- [2] A.O.Kluken and O. Grong: *Metall. Trans. A*, 1989, vol. 24A, p. 1335
- [3] S.S. Babu, S.A. David and T. DebRoy: *Sci. Tech. Weld. Join.*, 1996, vol. 1, p. 17
- [4] W.E Brower Jr.: Sc.D. Thesis, MIT, 1969
- [5] H. Goto, K. Miyazawa, W. Yamada and K. Tanaka: *ISIJ Int.*, 1995, vol.35, p.708
- [6] H. Goto, K. Yamaguchi, S. Ogibayashi and K. Miyazawa: *Tetsu-to-Hagane*, 1997, vol. 83, p. 833
- [7] J. Kunze, K-H. Spitzer, S. Oswald and C. Mickel: *Z. Metallkd.*, 1997, vol. 88, No. 3, p. 182
- [8] D. Turnbull and B. Vonnegut: *Ind. Eng. Chem.*, 1952, vol. 44, p. 1292
- [9] B.L. Bramfitt: *Metall. Trans.*, 1970, vol. 1, p. 1987
- [10] T. Ohashi, T. Hiromoto, H. Fuji, Y. Nuri and K. Asano: *Tetsu-to-Hagane*, 1976, vol. 62, p. 614
- [11] *Use of Fine Inclusions in Microstructure Control of Steels*, ISIJ, 1995, p. 8
- [12] O. Grong and D.K. Matlock: *Int. Met. Rev.*, 1986, vol. 31, p. 27
- [13] S. Ohkita and Y. Horii: *ISIJ int.*, 1995, vol. 35, p. 1170
- [14] R. E. Reed-Hill and R. Abbaschian: *Physical Metallurgy Principles*, 3rd ed., PWS Publishing Company, 1994, p. 679
- [15] F.B. Pickering: in *High Nitrogen Steels*, J. Foct and A. Hendry eds., Inst. Met., 1989, p. 10
- [16] T. Gladman: in *HSLA steels*, G. Tither and Z. Shouhua eds., TMS, 1992, p. 3
- [17] J.C. Villafuerte, H.W. Kerr and S.A. David: *Mat. Sci. Eng.*, 1995, vol. A194, p. 187
- [18] T. Koseki: *CAMP-ISIJ*, 1998, vol.11, p.530
- [19] T. Koseki, H. Inoue and M. Fuji: *Tetsu-to-Hagane*, to be published
- [20] Q.C. Bui: S.M. Thesis, MIT, 1998
- [21] D.R. Poirier and G.H. Geiger: *Transport Phenomena in Materials Processing*, TMS, 1994, p. 571

- [22] H. Muhlbach, G. Stephani, R. Sellger, and H. Fielder: *Int. J. Rapid Solidification*, 1987, vol. 3, p. 83
- [23] K. Takeshita and P. H. Shingu: *Trans. Jpn. Inst. Met.*, 1986, vol. 27, p. 454
- [24] M.J. Tenwick and H.A. Davies: in *Rapidly Quenched Metals V*, S. Steeb and H. Warlimont, eds., Elsevier, Publishers B.V., New York, NY, 1985, p. 67
- [25] W. Kurz & D. J. Fisher: *Fundamentals of Solidification*, 3rd ed., Trans Tech Publ., 1989, p. 293
- [26] M. Hirai, K. Kanamaru and H. Mori: in *Handbook of Iron and Steel*, Part 1, Maruzen Co. Ltd., Tokyo, 1981, p. 205
- [27] T.F. Bower, H.D. Brody and M.C. Flemings: *Trans. AIME*, 1966, vol. 233, p. 624
- [28] J. Chipman, Physical Chemistry of Steelmaking Committee, Iron and Steel Division, AIME: *Basic Open Hearth Steelmaking*, The American Institute of Mining and Metallurgical Engineering, 1951, p. 632
- [29] K. Hirano and Y. Ichihoshi: *Trans. Jpn. Inst. Met.*, 1968, vol. 32, p. 816
- [30] E. Ichise, R. Yamaba and T. Mori: *Proc. Int. Conf. Sci. & Technol. Iron & Steel, Tokyo*, 1970, section 3, p. 535
- [31] *Steelmaking Data Sourcebook, Revised ed.*, The 19th Committee on Steelmaking, The Japan Soc. for the Promotion of Sci., Gordon and Breach Science Publ., New York, NY, 1988
- [32] A. Suzuki, T. Suzuki, Y. Nagaoka and Y. Iwata: *Trans. Jpn. Inst. Met.*, 1968, vol. 32, p. 1302
- [33] M.C. Flemings: *Solidification Processing*, 1974, McGraw-Hill, New York, NY, p.117
- [34] D.M. Stefanescu, R.V. Phalnikar, H. Pang, S. Ahuja and B.K. Dhindaw: *ISIJ int.*, 1995, vol. 35, p. 700
- [35] H. Shibata, H. Yin, S. Yoshinaga, T. Emi and M. Suzuki: *ISIJ int.*, 1998, vol. 38, p. 149
- [36] M. Hua, C.I. Garcia and A.J. Deardo: *Metall. Trans. A*, 1997, vol. 28A, p. 1769
- [37] M. Volmer and A.Z. Weber: *Z. Phys. Chem.*, 1926, vol. 119, p. 227
- [38] D.Ya. Povolotskii, V.E. Roshchin and A.N. Keis: *Izv. Akad. Nauk SSSR, Metally*, 1970, vol. 5, p. 222
- [39] K. Schwerdtfeger: *Trans. AIME*, 1967, vol. 239, p. 134
- [40] C. Wagner: *Z. Electrochemie*, 1961, vol. 62, p. 581

Biographical Note

The author, Tomomitsu Inada, was born on October 10, 1967 in Sakaide City, Kagawa Prefecture, Japan. He graduated from Marugame High School in March, 1986, and entered the University of Tokyo in April of the same year. He majored in Physics and graduated in March, 1990, with the degree of Bachelor of Science. He joined Nippon Steel Corporation in April of the same year, and worked as an engineer for eight years (1990-1997) in the Steelmaking Division, Yawata Works. His work there was broad in scope, ranging from development of new techniques to the reduction of operation costs in the steelmaking and continuous casting processes. In September 1997, he entered the graduate school at MIT with a scholarship from Nippon Steel Corporation and joined the solidification group under the supervision of Professor Merton C. Flemings.